Taylor-vortex flow in shear-thinning fluids

S Topayev, C. Nouar, D Bernardin, A. Neveu, S A Bahrani

Taylor-vortex flow in shear-thinning fluids

S. Topayev, C. Nouar, D. Bernardin, A. Neveu and S.A. Bahrani

Université de Lorraine, LEMTA, UMR 7563,

Vandœuvre-lès-Nancy F-54500, France

CNRS, LEMTA, UMR 7563, Vandœuvre-lès-Nancy F-54500, France

(Dated: August 5, 2019)

Abstract

The present paper deals with the Taylor-Couette flow of shear-thinning fluids. It focuses on the first principles understanding the influence of the viscosity stratification and the nonlinear variation of the effective viscosity μ with the shear rate $\dot{\gamma}$ on the flow structure in the Taylor vortex flow regime. A wide gap configuration ($\eta = 0.4$) is mainly considered. A weakly nonlinear analysis, using the amplitude expansion method at high order is adopted as a first approach to study nonlinear effects. For the numerical computation, the shear-thinning behavior is described by the Carreau model. The rheological parameters are varied in a wide range. The results indicate that the flow field undergoes a significant change as shear-thinning effects increase. First, vortices are squeezed against the inner wall and the center of the patterns are shifted axially towards the radial outflow boundaries ($z = 0$, $z/\lambda_z = 1$). This axial shift leads to increasing concentration of vorticity at these positions. The outflow becomes more stronger than the inflow and the inflow zone, where the vorticity is low, increases accordingly. Nevertheless, the strength of the vortices relative to the velocity of the inner cylinder is weaker. Second, the pseudo-Nusselt number, ratio of the torque to that obtained in the laminar flow, decreases. Third, higher harmonics become more relevant and grow faster with Reynolds number. Finally, the modification of the viscosity field is described.

I. INTRODUCTION

Instabilities of Couette flow between two coaxial cylinders are considered as prototypes for general studies in hydrodynamic instability and transition to turbulence. A survey of the literature on the Taylor-Couette problem can be found in Koschmieder [1] and Tagg [2]. In the classical configuration, the inner cylinder is rotating and the outer one is fixed. The basic state, a circular Couette-flow (CCF), is purely azimuthal with a balance between the centrifugal force and the pressure gradient pointing inward. In this situation, the angular momentum decreases with the radius. According to Rayleigh criterion [3], CCF is unstable in the inviscid limit with respect to axisymmetric three-dimensional perturbation. Taylor [4] determined theoretically and experimentally the influence of the fluid viscosity on the stability boundary. The primary instability results in axisymmetric meridional rolls (Taylor vortices) periodically spaced in the axial direction and separated by radial jets. When the inner cylinder rotation rate is increased, a Hopf bifurcation to a rotating wave occurs, i.e. the Taylor vortex flow (TVF) acquires a periodicity along the azimuthal direction θ. The resulting state is the wavy vortex flow (WVF). The Reynolds number $\mathcal{R}$ for onset of time-dependent wavy vortices was computed numerically by Jones [5]. It is shown that for a radius ratio, $\eta = R_1/R_2$, close to 1, say $\eta \geq 0.85$, the supercritical Reynolds number regime in which the axisymmetric vortices are stationary is very small. As the radius ratio is decreased, the wavy vortices set in at higher and higher Reynolds numbers. This result was confirmed experimentally. For instance, in experiments performed by Snyder & Lambert [6] with a gap of radius ratio $R_1/R_2 = 0.5$, the first appearance of significant azimuthal waviness was reported at $\mathcal{R} \approx 10\,\mathcal{R}_c$. Furthermore, they suggested that this was probably due to end effects of the cylinders. For the same radius ratio, i.e. $\eta = 0.5$, Meincke & Egbers [7] observed experimentally a transition to WVF at $\mathcal{R} \approx 16\,\mathcal{R}_c$. Thus, from experimental point of view, it is not clear at which Reynolds number the flow in a wide gap undergoes a transition to wavy-mode. The disagreement between experimental results could be related to the influence of the aspect ratio (AR = column length/gap width). Indeed in [6] $AR \approx 30$, whereas in [7], $AR \approx 4$.

For moderate or small gap width (say $\eta > 0.75$), increasing further $\mathcal{R}$, the system undergoes a bifurcation from wavy-vortex-flow (WVF) to modulated wavy-vortex-flow (MWVF), characterized by the presence of a second frequency modulating the rotating waves as described by Andereck *et al.* [8]. Subsequent bifurcations lead generally to turbulence after few steps.

This orderly progression of nonlinear flow states makes Taylor-Couette flow as an attractive model for studying transition to turbulence.

In the case of non-Newtonian fluids (polymer solutions, suspensions, emulsions, ...), mechanisms of the instability and transition to turbulence may be modified by the nonlinearity of the rheological behavior. Most non-Newtonian fluids have two common properties, viscoelasticity and shear-thinning. Polymer solutions, colloïdal suspensions as well as particulate dispersions display this behavior above a certain concentration threshold. There was a significant interest in inertialess viscoelastic Taylor-Couette instability since the pioneering work of Giesekus [9]. This instability was then analyzed by Muller *et al.* [10], Larson *et al.* [11] and Shaqfeh *et al.* [12]. In the laminar state, the rotation produces a shear which stretches the polymer molecule along the curved stream lines. This leads to a first normal stress difference which acts against the centrifugal force. Groisman and Steinberg (1998) [13] showed experimentally that elastic instability leads to a strong nonlinear flow transition at vanishing inertia.
Hereafter, we focus on shear-thinning fluids, for which the elastic response can be neglected. Typically, stiff polymer solutions, show significant nonlinear decrease of the viscosity with the shear-rate, with almost negligible elastic effects [14]. The shear-thinning behavior, i.e. a nonlinear decrease of the viscosity with the shear rate, arises from the reorganization of the internal fluid structure to reduce the viscous dissipation. The characteristic time of the reorganization of the flow structure is supposed much smaller than all characteristic times of the problem. In other words, the fluid is assumed purely viscous and its response to an applied shear-stress is instantaneous.

I.1. Brief Review on Taylor-Couette flow of shear-thinning fluids

Circular Couette flow of a shear-thinning fluid is mainly characterized by a viscosity stratification in the annular space, which is more significant as the shear-thinning effects are stronger and the annular space is wider. With increasing shear-thinning effects, the shear rate increases at the inner wall and decreases at the outer one. Furthermore, the nonlinear variation of the viscosity with the shear rate introduces at the linear level an anisotropy in the deviatoric tensor associated to the perturbation. This latter point is discussed in section II.4.

The mechanism of instability of CCF of shear-thinning fluids is the same as for a Newtonian fluid and results in axisymmetric counter rotating vortices separated by radial inflow and outflow jets of angular momentum emanating from the fluid layers adjacent to the cylinders' wall. However, the critical conditions are different because of the radial viscosity stratification and the modification of the azimuthal velocity profile. In the case where the inner cylinder is rotating and the outer one is at rest, the critical Reynolds and axial wave numbers are given in the literature for power-law and Carreau fluids, for wide and narrow annular spaces, see for instance Agbessi *et al* [15] and Alibenyahia *et al* [16] and the references therein. When both the inner and the outer cylinders are rotating, the critical conditions were determined by Agbessi *et al* [15] for a narrow and a wide annular space. It is shown that when the Reynolds number is defined using the inner wall-shear viscosity, the shear-thinning delays the appearance of Taylor vortices. It is explained that this delay is due to the reduction of the energy exchange between the base flow and the perturbation. A radically different conclusion may be reached if one uses the zero-shear viscosity of the fluid as viscosity scale. In the narrow gap-limit and weakly shear-thinning behavior of the fluid, Li & Khayat [17] found that the critical Reynolds number defined with the zero-shear viscosity becomes lower as shear-thinning effects increase. Similar tendency is observed when free (slip) boundary conditions are used [18–20]. Recently Masuda *et al.* [21] suggested to use an average viscosity weighted by the strain-rate squared. They found that the critical Reynolds number defined with this average viscosity is the same as for a Newtonian fluid. However, this result is limited only to a narrow annular space with a radius ratio $\eta > 0.7$.
From experimental point of view, Escudier *et al.* [22] suggested to determine the critical conditions by focusing on the development of the axial velocity component, near the inner wall at a radial position r such $(R_2 - r)/(R_2 - R_1) = 0.8$.
Sinevic et al. [23] measured the torque acting on the inner cylinder for three shear-thinning fluids described by a power-law model ($n_p = 0.4$, 0.45 and 0.57). They found that in the Taylor-vortex flow region, the power number Po behaves as $Po \propto Re_w^{-0.7}$, where, Re_w is the Reynolds number defined with the inner wall shear-viscosity. Concerning the flow structure, for a wide gap, it is shown theoretically [15, 16] and experimentally [22] that with increasing shear-thinning effects, the vortex eye is shifted toward the inner cylinder, because of the viscosity stratification: the viscosity increases from the inner cylinder to the outer one. Escudier *et al.* [22] investigated the flow structure in a Taylor-Couette geometry with a radius ratio of 0.5. Axial and tangential velocity measurements were made using Laser Doppler

Anemometry for a 0.15% aquesous solution of xanthan gum, whose rheological behavior is described by a power-law model with a shear-thinning index $n_p \approx 0.45$. The results show an axial shift of the vortices towards the radial outflow boundary slightly more pronounced for a shear-thinning fluid than for a Newtonian fluid. Except for this issue dealing with the position of the vortex, results are very sparse. For instance, there is no indication on the influence of shear-thinning effects on the strength of the radial outflow and radial inflow, nor on the azimuthal streaks in outflow and inflow regions, nor on the modification of the viscosity field by Taylor vortices particularly in a wide annular space and strong shear-thinning effects. It is clear that a more clear understanding and characterization of supercritical Taylor vortex flow of a shear-thinning fluid is needed.

To our best knowledge, there are no theoretical nor numerical studies on shear-thinning effects in Taylor vortex flow structure.

I.2. Objectives, methodology and outline of the paper

The objective of the present work is to examine the effects of the nonlinear relation between the viscosity and the shear rate on the flow structure, the viscosity field and the torque applied on the inner cylinder. Actually, there is an interplay between nonlinear inertia terms and nonlinear viscous terms. Based on the experimental results such the streamline patterns in Taylor vortices represented by Escudier et al. [22] and the spatiotemporal plots reported by Cagney and Balabani [24] for different shear-thinning fluids, the Taylor vortex flow observed can be considered as periodic with a wavenumber k close to the critical value k_c. Here we take $k = k_c$ and we concentrate on solutions that consist of this mode plus modes that can be generated from it through the nonlinearity. A weakly nonlinear analysis based on the amplitude expansion method is used as a first approach to study nonlinear effects. This method was pioneered by Watson [25] and Stuart [26] who used such expansion to describe the subcritical modes in plane Poiseuille flow below the linear instability threshold. Herbert [27] and Sen & Venkateswarlu [28] improved Watson's expansion method by making a definition of the disturbance amplitude clear. An other alternative is the multiple scales method. Fujimura [29] demonstrated the complete equivalence between these two methods. Here, we focus on the case of a wide gap with $\eta = 0.4$, where shear-thinning are more pronounced. The case of a narrow gap is briefly discussed in the last section.

The article is organized as follows. In § 2, we formulate the physical problem, state the

governing equations and define the dimensionless parameters. The velocity and viscosity profiles of the base state are discussed and the perturbation equations are derived. Subsequently, the linear stability analysis is presented in section 3. In § 4, the main steps of the weakly nonlinear analysis are outlined. The results are presented and discussed in § 5. The contribution of the nonlinear viscous terms on the saturated coefficient at cubic order in the amplitude equation is analysed. Departing from the onset, the weakly nonlinear analysis is carried out up to seventh-order in the amplitude equation. The influence of shear-thinning effects on the flow structure, the viscosity field and the torque applied on the inner cylinder is highlighted. Finally, § 6 is devoted to a concluding discussion.

II. PHYSICAL AND MATHEMATICAL MODEL

II.1. Basic formulation

We consider the flow of an incompressible shear-thinning fluid between two coaxial cylinders of inner and outer radii $\hat{R}_1$ and $\hat{R}_2$ respectively. The radius ratio is $\eta = \hat{R}_1/\hat{R}_2$. The outer cylinder is at rest and the inner cylinder rotates with an angular velocity $\hat{\Omega}_1$. The cylinders are assumed to be infinite. The incompressibility condition and the momentum equations read

$$\mathbf{div}\,\boldsymbol{U} = 0 \tag{1}$$

$$\partial_t \boldsymbol{U} + \mathcal{R}\,(\boldsymbol{\nabla U})\cdot\boldsymbol{U} = -\boldsymbol{\nabla} P + \mathbf{div}\,(\boldsymbol{\tau})\ , \tag{2}$$

where $\boldsymbol{U} = U\mathbf{e}_r + V\mathbf{e}_\theta + W\mathbf{e}_z$ is the velocity vector in cylindrical coordinates (r,θ,z), P a generalized pressure which includes the effect of gravity, $\hat{\boldsymbol{\tau}}$ the deviatoric extra-stress tensor, and $\mathcal{R}$ is the Reynolds number:

$$\mathcal{R} = \hat{\rho}\,\hat{\Omega}_1\hat{R}_1\hat{d}/\hat{\mu}_0\,. \tag{3}$$

The quantities defined with a hat ($\hat{.}$) are dimensional, while quantities without ($\hat{.}$) are dimensionless. To scale these equations, we have followed Chossat & Iooss [30], with the aim of maintaining some compatibility between the notations used here and those found in the literature for Newtonian fluids. Lengths are scaled with the annular gap $\hat{d} = \hat{R}_2 - \hat{R}_1$. Velocities are scaled with $\hat{R}_1\hat{\Omega}_1$. Time is scaled with a viscous diffusion time $\hat{\rho}\,\hat{d}^2/\hat{\mu}_0$, where $\hat{\rho}$ and $\hat{\mu}_0$ are the density a characteristic viscosity of the fluid. The pressure and the deviatoric stress are scaled with $\hat{\mu}_0\hat{R}_1\hat{\Omega}_1/\hat{d}$. To the previous equations, we add the no-slip and

impermeability conditions at the walls,

$$U = W = 0,\, V = 1 \quad \text{at} \quad r = R_1, \tag{4}$$

$$U = V = W = 0 \qquad \text{at} \quad r = R_2, \tag{5}$$

where $R_1 = \eta/(1-\eta)$ and $R_2 = 1/(1-\eta)$. The fluid is assumed to be purely viscous. The constitutive equation reads:

$$\boldsymbol{\tau} = \mu(\mathcal{R}, \Gamma)\dot{\boldsymbol{\gamma}} \quad \text{with} \quad \dot{\boldsymbol{\gamma}} = \boldsymbol{\nabla U} + (\boldsymbol{\nabla} U)^T \,, \tag{6}$$

where the second invariant of the strain-rate tensor is expressed as

$$\Gamma = \frac{1}{2}\,\dot{\boldsymbol{\gamma}} \colon \dot{\boldsymbol{\gamma}} = \frac{1}{2}\dot{\gamma}_{ij}\dot{\gamma}_{ij}\,. \tag{7}$$

In Equation 7, the Einstein's summation convention for repeated indices is used.

II.2. Carreau model

Although the equations derived here are valid for any nonlinear purely viscous fluid, for numerical applications, a rheological model has to be chosen to describe the shear-thinning behavior. We have chosen the Carreau model [31] because it has a sound theoretical basis and is C^∞ with respect to Γ, unlike the power-law model or Carreau-Yasuda model which are singular at $\Gamma = 0$. The Carreau's law reads [32]

$$\frac{\hat{\mu} - \hat{\mu}_\infty}{\hat{\mu}_0 - \hat{\mu}_\infty} = \left(1 + \hat{\lambda}^2\hat{\Gamma}\right)^{(n_c-1)/2} \,, \tag{8}$$

where $\hat{\mu}_0$ and $\hat{\mu}_\infty$ are the dynamic viscosity at low and high shear rate, $n_c < 1$ the shear-thinning index and $\hat{\lambda}$ the characteristic time of the fluid. The location of the transition from the Newtonian plateau to the shear-thinning regime is determined by $\hat{\lambda}$ since $1/\hat{\lambda}$ defines the characteristic shear rate for the onset of shear-thinning. Increasing $\hat{\lambda}$ reduces the Newtonian plateau to lower shear rates. The infinite shear viscosity $\hat{\mu}_\infty$ is generally associated with the breakdown of the fluid and is frequently significantly smaller, $(10^3 - 10^4)$ times smaller than $\hat{\mu}_0$ see Bird *et al* [32] and Tanner [33]. The ratio $\hat{\mu}_\infty/\hat{\mu}_0$ will be thus neglected in the following. This leaves three rheological parameters: $\hat{\mu}_0$, $\hat{\lambda}$ and n_c. The Newtonian behavior, $\hat{\mu} = \hat{\mu}_0$ is recovered by setting $n_c = 1$ or $\hat{\lambda} = 0$. It is interesting to note that when the characteristic time $\hat{\lambda}$ of the fluid is larger than the advection time $\left(\hat{d}/\hat{R}_1\right)\,\hat{\Omega}_1^{-1}$, the Carreau model tends towards the power-law model $\hat{\mu} = \hat{K}\hat{\Gamma}^{(n_c-1)/2}$ with a consistency

$\hat{K} = \hat{\mu}_0 \hat{\lambda}^{(n_c-1)/2}$. Examples of the values of the Carreau parameters can be found in the literature, particularly for solutions of xanthan gum, stiff-rode-like polymer [21, 34, 35]. Typically, the characteristic time of the fluid $\hat{\lambda}$ is of order of seconds or tens of seconds and the zero shear viscosity is of order 0.1 Pa.s or 10 Pa.s. The shear thinning index $n_c \in]0, 1[$. In dimensionless form the Carreau's law reads

$$\mu\left(\mathcal{R}, \Gamma\right) = \frac{\hat{\mu}}{\hat{\mu}_0} = \left[1 + \left(\lambda \mathcal{R}\right)^2 \Gamma\right]^{\frac{n_c-1}{2}} \quad \text{with} \quad \lambda = \frac{\hat{\lambda}}{\hat{\rho}\, \hat{d}^2/\hat{\mu}_0}. \tag{9}$$

II.3. Base flow

For sufficiently small Reynolds number, the circular Couette flow is a solution of the system (1), (2), satisfying the boundary conditions (4) and (5). It is given by :

$$\boldsymbol{U}_b = (0, V_b(r), 0) \quad , \quad \frac{d}{dr}\left(r^2 \tau_{r\theta_b}\right) = 0 \quad \text{with} \quad V_b(R_1) = 1 \ \text{and} \ V_b(R_2) = 0\,, \tag{10}$$

where,

$$\tau_{r\theta b} = \mu_b \left(\frac{dV_b}{dr} - \frac{V_b}{r}\right) \quad \text{with} \quad \mu_b = \mu\left(\mathcal{R}, \Gamma_b\right) = \left[1 + \left(\lambda \mathcal{R}\right)^2 \Gamma_b\right]^{(n_c-1)/2}\,. \tag{11}$$

The system (10), (11) is solved numerically using an iterative process combined with a polynomial Chebyshev approximation of the azimuthal velocity profile [15, 16]. One must notice that contrarily to the Newtonian case, for a non-Newtonian fluid, the dimensionless base flow $\boldsymbol{U}_b$ also depends on $\mathcal{R}$. However, for the sake of simplicity, this dependence is left implicit. Figure 1 shows the effect of the shear-thinning index on the velocity and viscosity profiles at $\eta = 0.4$ and $\lambda\mathcal{R} = 100$. With increasing shear-thinning effects, the curvature of the velocity profile becomes more pronounced. The shear rate increases at the inner wall and decreases at the outer one. This results in a viscosity stratification within the gap. The viscosity as well as the degree of viscosity stratification defined by $d\mu_b/dr$ increases from the inner to the outer wall. For sufficiently strong shear-thinning effects, a thick layer of the fluid with low shear-rate and large viscosity forms at the outer wall as shown by the curve (4) in Fig. 1(b). In the figure 1(a), the velocity profiles are almost the same as those obtained for a power-law fluid,

$$V_b(r) = \frac{r}{R_1}\left[1 - \left(\frac{1}{R_2^{2/n_p}} - \frac{1}{R_1^{2/n_p}}\right)^{-1}\left(\frac{1}{r^{2/n_p}} - \frac{1}{R_1^{2/n_p}}.\right)\right] \tag{12}$$

It is the same for the viscosity profiles except for $n_c = 0.2$ and $\eta = 0.4$, where a difference is observed near the outer cylinder. Actually at $\eta = 0.4$, the numerical results show that there

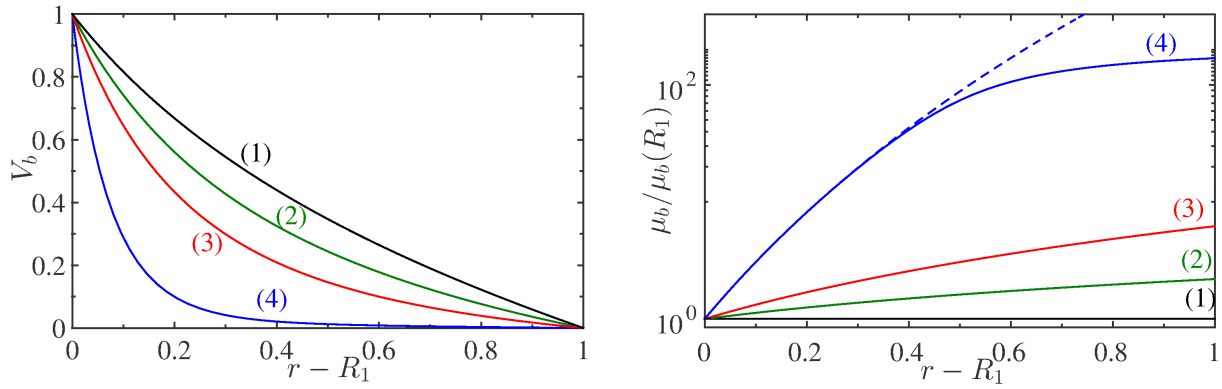

(a) **(b)**

FIG. 1: (Color online) Base flow for Carreau fluids at $\eta = 0.4$ and $\lambda\mathcal{R} = 100$. Influence of shear-thinning index n_c on the velocity **(a)** and viscosity **(b)** profiles. (1) $n_c = 1$ (Newtonian fluid); (2) $n_c = 0.7$; (3) $n_c = 0.5$ and (4) $n_c = 0.2$. Dashed line is the viscosity profile for a power-law fluid with $n_p = 0.2$.

is no significant difference between Carreau and power-law velocity profiles when $\lambda\mathcal{R} \geq 10$. However, for the viscosity profiles a larger value of $\lambda\mathcal{R}$ is needed to reduce the difference observed near the outer cylinder, particularly for low values of n_c.

II.4. Perturbation equations

The velocity $\boldsymbol{U}$ and the pressure P are splitted into the basic field (with the subscript b) and the disturbance:

$$\boldsymbol{U} = \boldsymbol{U}_b + \boldsymbol{u} \qquad \text{and} \qquad P = P_b + p\,. \tag{13}$$

Substituting $\boldsymbol{U}$ and P by their expressions in (1) and (2) leads to

$$\boldsymbol{\nabla} \cdot u = 0\,, \tag{14}$$

$$\partial_t \mathbf{u} = -\mathcal{R}\left[\mathbf{u} \cdot \boldsymbol{\nabla}\mathbf{u} + \boldsymbol{U}_b \cdot \boldsymbol{\nabla}\boldsymbol{u} + \boldsymbol{u} \cdot \boldsymbol{\nabla}\boldsymbol{U}_b\right] - \boldsymbol{\nabla} p + \boldsymbol{\nabla} \cdot \left(\boldsymbol{\tau}(\boldsymbol{U}_b + \boldsymbol{u}) - \boldsymbol{\tau}(\boldsymbol{U}_b)\right)\,, \tag{15}$$

where, $\tau_{ij}\left(\boldsymbol{U}_b + \boldsymbol{u}\right) = \mu\left(\boldsymbol{U}_b + \boldsymbol{u}\right)\dot{\gamma}_{ij}\left(\boldsymbol{U}_b + \boldsymbol{u}\right)$. The boundary conditions are:

$$\boldsymbol{u} = 0 \qquad \text{and} \qquad \partial_r(\boldsymbol{u} \cdot \boldsymbol{e}_r) = 0 \quad \text{at} \quad r = R_1,\, R_2\,. \tag{16}$$

The second condition arises from the continuity equation. For a small amplitude disturbance, the viscosity of the perturbed flow can be expanded around the base flow as:

$$\mu\left(\boldsymbol{U}_b+\boldsymbol{u}\right)=\mu_b+\mu_1\left(\boldsymbol{u}\right)+\mu_2\left(\boldsymbol{u},\boldsymbol{u}\right)+\mu_3\left(\boldsymbol{u},\,\boldsymbol{u},\,\boldsymbol{u}\right)+\ldots, \tag{17}$$

where,

$$\mu_1\left(\boldsymbol{u}\right)=\left[\frac{\partial\mu}{\partial\dot{\gamma}_{ij}}\right]_b\dot{\gamma}_{ij}\left(\boldsymbol{u}\right), \tag{18}$$

$$\mu_2\left(\boldsymbol{u},\,\boldsymbol{u}\right)=\frac{1}{2}\left[\frac{\partial^2\mu}{\partial\dot{\gamma}_{ij}\partial\dot{\gamma}_{k\ell}}\right]_b\dot{\gamma}_{ij}\left(\boldsymbol{u}\right)\dot{\gamma}_{k\ell}\left(\boldsymbol{u}\right), \tag{19}$$

$$\mu_3\left(\boldsymbol{u},\,\boldsymbol{u},\,\boldsymbol{u}\right)=\frac{1}{6}\left[\frac{\partial^3\mu}{\partial\dot{\gamma}_{ij}\partial\dot{\gamma}_{k\ell}\partial\dot{\gamma}_{pq}}\right]_b\dot{\gamma}_{ij}\left(\boldsymbol{u}\right)\dot{\gamma}_{k\ell}\left(\boldsymbol{u}\right)\dot{\gamma}_{pq}\left(\boldsymbol{u}\right), \tag{20}$$

The deviatoric stresses in the disturbed flow can also be written as

$$\tau_{ij}\left(\boldsymbol{U}_b+\boldsymbol{u}\right)=\tau_{ij}\left(\boldsymbol{U}_b\right)+\tau_{1,ij}\left(\boldsymbol{u}\right)+\tau_{2,ij}\left(\boldsymbol{u},\boldsymbol{u}\right)+\tau_{3,ij}\left(\boldsymbol{u},\,\boldsymbol{u},\,\boldsymbol{u}\right)+\ldots, \tag{21}$$

with,

$$\tau_{1,ij}\left(\boldsymbol{u}\right)=\mu_b\dot{\gamma}_{ij}\left(\boldsymbol{u}\right)+\mu_1\left(\boldsymbol{u}\right)\dot{\gamma}_{ij}(\boldsymbol{U}_b), \tag{22}$$

$$\tau_{2,ij}\left(\boldsymbol{u},\,\boldsymbol{u}\right)=\mu_2\left(\boldsymbol{u}\,,\boldsymbol{u}\right)\dot{\gamma}_{ij}\left(\boldsymbol{U}_b\right)+\mu_1\left(\boldsymbol{u}\right)\dot{\gamma}_{ij}\left(\boldsymbol{u}\right), \tag{23}$$

$$\tau_{3,ij}\left(\boldsymbol{u},\,\boldsymbol{u}\right)=\mu_3\left(\boldsymbol{u}\,,\boldsymbol{u}\,,\boldsymbol{u}\right)\dot{\gamma}_{ij}\left(\boldsymbol{U}_b\right)+\mu_2\left(\boldsymbol{u},\,\boldsymbol{u}\right)\dot{\gamma}_{ij}\left(\boldsymbol{u}\right). \tag{24}$$

In the case of a circular Couette flow of a viscous fluid, we have $\dot{\gamma}^b_{ij}=0$, if $ij\neq r\theta$, θr and $\dot{\gamma}^b_{r\theta}=DV^b-V^b/r$, where $D\equiv d/dr$. Setting $\Gamma_b=\left(\dot{\gamma}^b_{r\theta}\right)^2$ and $\Gamma_2=(1/2)\dot{\gamma}_{ij}(\boldsymbol{u})\dot{\gamma}_{ij}(\boldsymbol{u})$, the expressions of μ_1,μ_2 and μ_3 can be simplified,

$$\mu_1=2\left[\frac{d\mu}{d\Gamma}\right]_b\dot{\gamma}^b_{r\theta}\dot{\gamma}_{r\theta}(\boldsymbol{u}), \tag{25}$$

$$\mu_2=\left[\frac{d\mu}{d\Gamma}\right]_b\Gamma_2+2\left[\frac{d^2\mu}{d\Gamma^2}\right]_b\Gamma_b\dot{\gamma}^2_{r\theta}(\boldsymbol{u}), \tag{26}$$

$$\mu_3=2\left[\frac{d^2\mu}{d\Gamma^2}\right]_b\dot{\gamma}^b_{r\theta}\dot{\gamma}_{r\theta}(\boldsymbol{u})\Gamma_2+\frac{4}{3}\left[\frac{d^3\mu}{d\Gamma^3}\right]_b\left(\dot{\gamma}^b_{r\theta}\right)^3\dot{\gamma}^3_{r\theta}(\boldsymbol{u}). \tag{27}$$

Replacing μ_1, μ_2, μ_3 by their expressions (25)-27) into equations (22)-(24), we obtain

$$\tau_{1,ij}=\mu_b\dot{\gamma}_{ij}(\boldsymbol{u})\qquad\text{if}\qquad ij\neq r\theta,\theta r, \tag{28}$$

$$\tau_{1,r\theta}=\left[\mu_b+2\left(\frac{d\mu}{d\Gamma}\right)_b\left(\dot{\gamma}^b_{r\theta}\right)^2\right]=\mu_t\dot{\gamma}_{r\theta}(\boldsymbol{u}), \tag{29}$$

$$\tau_{2,ij}=\mu_1\dot{\gamma}_{r\theta}(\boldsymbol{u})\qquad\text{if}\qquad ij\neq r\theta,\theta r, \tag{30}$$

$$\tau_{2,r\theta}=\mu_2\dot{\gamma}^b_{r\theta}+\mu_1\dot{\gamma}_{r\theta}(\boldsymbol{u}), \tag{31}$$

$$\tau_{3,ij}=\mu_2\dot{\gamma}_{r\theta}(\boldsymbol{u})\qquad\text{if}\qquad ij\neq r\theta,\theta r, \tag{32}$$

$$\tau_{3,r\theta}=\mu_3\dot{\gamma}^b_{r\theta}+\mu_2\dot{\gamma}_{r\theta}(\boldsymbol{u}). \tag{33}$$

In equation (29), μ_t is the tangent viscosity. For one dimensional shear flow with the velocity $V_b(r)$ in the azimuthal direction, the tangent viscosity is given by $\mu_t = (\partial\mu/\partial\dot{\gamma}_{r\theta})_b$. Note that for simplicity of writing, we preferred to write the viscosity as a function of $\boldsymbol{U_b}$ and $\boldsymbol{u}$ rather than $\mathcal{R}, \Gamma_b$ and Γ_2.

Here, we consider axisymmetric disturbances. For generalized Newtonian fluids and in the case where the outer cylinder is fixed and the inner one is rotating, the numerical tests performed by Alibenyahia *et al* [16] and Agbessi *et al* [15], for a large range of rheological parameters, showed that the least stable mode is axisymmetric. In this case, the continuity simplifies and is satisfied via introduction of a streamfunction ψ

$$u = -\frac{1}{r}\frac{\partial\psi}{\partial z} \quad \text{and} \quad w = \frac{1}{r}\frac{\partial}{\partial r}(\psi)\,. \tag{34}$$

However, it is found that it is more convenient to work with $\phi = \dfrac{\psi}{r}$ in terms which

$$u = -\frac{\partial\phi}{\partial z} \quad \text{and} \quad w = \frac{1}{r}\frac{\partial}{\partial r}(r\phi) \tag{35}$$

Cross-differentiating r- and z- momentum equations and eliminating the pressure, we obtain

$$\begin{aligned}\frac{\partial\Omega}{\partial t} = \mathcal{R}\left[\frac{\partial\phi}{\partial z}D\Omega - D_*\phi\frac{\partial\Omega}{\partial z} - \frac{1}{r}\frac{\partial\phi}{\partial z}\Omega - \frac{2}{r}v\frac{\partial v}{\partial z} - 2\frac{V_b}{r}\frac{\partial v}{\partial z}\right] + \\ \left(DD_* - \frac{\partial^2}{\partial z^2}\right)\tau_{rz} + \frac{\partial}{\partial z}\left(D\tau_{zz} - D_*\tau_{rr} + \frac{\tau_{\theta\theta}}{r}\right)\end{aligned} \tag{36}$$

$$\frac{\partial v}{\partial t} = \mathcal{R}\left(\frac{\partial\phi}{\partial z}D_*v - D_*\phi\frac{\partial v}{\partial z} + \frac{\partial\phi}{\partial z}D_*V_b\right) + \frac{1}{r^2}D\left(r^2\tau_{r\theta}\right) + \frac{\partial}{\partial z}\tau_{\theta z}\,, \tag{37}$$

where, $D \equiv \dfrac{\partial}{\partial r}$, $D_* \equiv D + \dfrac{1}{r}$ and $\Omega = \left(DD_* + \dfrac{\partial^2}{\partial z^2}\right)\phi$ the azimuthal vorticity.

III. LINEAR STABILITY ANALYSIS

The linearized version of the disturbance equations (36) and (37) is

$$\frac{\partial\Omega}{\partial t} = -2\mathcal{R}\frac{V_b}{r}\frac{\partial v}{\partial z} + \left(DD_* - \frac{\partial^2}{\partial z^2}\right)\tau_{1,rz} + \frac{\partial}{\partial z}\left(D\tau_{1,zz} - D_*\tau_{1,rr} + \frac{\tau_{1,\theta\theta}}{r}\right)\,, \tag{38}$$

$$\frac{\partial v}{\partial t} = \mathcal{R}(D_*V_b)\frac{\partial\phi}{\partial z} + \frac{1}{r^2}D\left(r^2\tau_{1,r\theta}\right) + \frac{\partial}{\partial z}\tau_{1,\theta z}\,. \tag{39}$$

III.1. Direct mode

Using the invariance of equations (38), (39) (by translation along the axial direction, reflection $z \to -z$), we seek the eigenmodes in the following form:

$$(\phi,\, v) = (F_{11}(r),\, V_{11}(r)) \exp\left(st + ikz\right) , \tag{40}$$

where $k \in \mathbb{R}$, is the axial wavenumber and $s = s_r + is_i$ a complex eigenvalue. Its real part s_r is the growth-rate of the disturbance and the imaginary part allows to define the axial phase velocity. Substituting (40) into (38) and (39):

$$s\left(DD_* - k^2\right) F_{11} = -2ik\mathcal{R}\frac{V_b}{r}V_{11} + \left(DD_* - k^2\right)\left[\mu_b\left(DD_* - k^2\right) F_{11}\right] + 2k^2\left(D^2\mu_b\right) F_{11} , \tag{41}$$

$$sV_{11} = ik\mathcal{R}\left(D_*V_b\right) F_{11} + \frac{1}{r^2}D\left[r^2\mu_t\left(DV_{11} - \frac{V_{11}}{r}\right)\right] - k^2\mu_b V_{11} , \tag{42}$$

with

$$F_{11} = DF_{11} = V_{11} = 0 \quad \text{at} \quad r = R_1, R_2 . \tag{43}$$

The set of differential equations (41) and (42) is an eigenvalue problem where s is an eigenvalue and $\boldsymbol{X}_{11} = (F_{11}, V_{11})$ the eigenvector. It can be written formally as

$$s\boldsymbol{M} \cdot \boldsymbol{X}_{11} = \boldsymbol{L} \cdot \boldsymbol{X}_{11} . \tag{44}$$

Since any multiple of the eigenvector $\boldsymbol{X}_{11}$ is also solution of (43), $\boldsymbol{X}_{11}$ can be normalized such that

$$\max(V_{11}) = 1. \tag{45}$$

The eigenvalue problem (44) with the boundary conditions (43) is solved using a spectral collocation method based on Chebyshev polynomials evaluated at $N+1$ collocation points of the Gauss-Lobatto method. The matrix eigenvalue problem that results is solved using QZ algorithm with Matlab. To test the convergence of the numerical method, the computations of the critical conditions are made with different spectral truncation N. It is observed that 40 collocation points provide sufficient accuracy for the rheological parameters considered here. The results given in the paper are obtained with $N = 50$. Marginal stability curves are determined for different rheological parameters (n_c and λ). The minimum of these curves gives the critical conditions $\mathcal{R}_c$ and k_c. In Figure 2, normalized marginal stability curves, $\mathcal{R}/\mathcal{R}_c$ vs

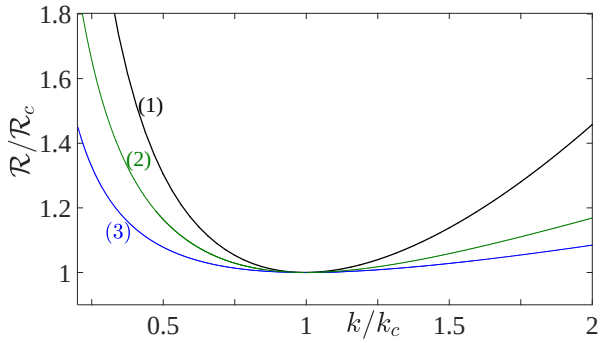

FIG. 2: (Color online) Normalized marginal stability curves at $\eta = 0.4$ for a Newtonian fluid (1) where $\mathcal{R}_c = 68.3$, and $k_c = 3.183$ and Carreau fluids: (2) $n_c = 0.5$, $\lambda = 1$, $\mathcal{R}_c = 16.57$, $k_c = 3.487$; (3) $n_c = 0.2$, $\lambda = 44$, $\mathcal{R}_c = 2.282$, $k_c = 8.355$.

k/k_c are shown for a Newtonian fluid and for Carreau fluids. It is interesting to observe that the marginal stability curves flatten with increasing shear-thinning effects. The curvature at threshold allows to define the coherence length of perturbations $\xi_0 = \dfrac{1}{2\mathcal{R}_c}\left(\dfrac{\partial^2\mathcal{R}}{\partial k^2}\right)_{\mathcal{R}_c,k_c}$. To evaluate the second derivative, we have followed the methodology described in [36]. The variation of ξ_0 as a function of the shear-thinning index n_c for different values of λ is shown in figure 3. It can be observed that the coherence length of perturbations decreases with decreasing n_c. This effect is particularly significant for very low values of n_c.

A second feature of shear-thinning effects is highlighted by eigenvalues spectra. They are shown in Fig. 4 at the critical conditions with $\eta = 0.4$, for a Newtonian and a Carreau-fluid with $n_c = 0.2$ and $\lambda = 44$. The eigenvalues are real or complex conjugate [37]. However, the first eigenvalue that crosses the real axis is always real in agreement with the principle of stability exchange [37]. One can note that with increasing shear-thinning effects, the relaxation times of the eigenmodes become closer one to another. For instance, for a Newtonian fluid at the critical conditions, the first eigenvalue is $s_1 = -8.0 \times 10^{-6}$ and the second one is $s_2 = -44.5$ while for a Carreau fluid with $n_c = 0.2$, $\lambda = 44$, we have $s_1 = -1.808 \times 10^{-6}$ and $s_2 = -1.726$. The variation of the critical Reynolds number as a function of the shear-thinning index n_c, at $\eta = 0.4$ is shown in figure 5(a) for different values of the dimensionless characteristic time λ. With the definition (3) of $\mathcal{R}$, the influence of shear-thinning appears destabilizing. Opposite effects can be found by using a Reynolds number defined with the viscosity μ_{bw} evaluated at the inner wall, $\mathcal{R}_w = \mathcal{R}/\mu_{bw}$. The selection of the viscosity scale may be considered a matter of choice, however the conclusion that one reaches by compar-

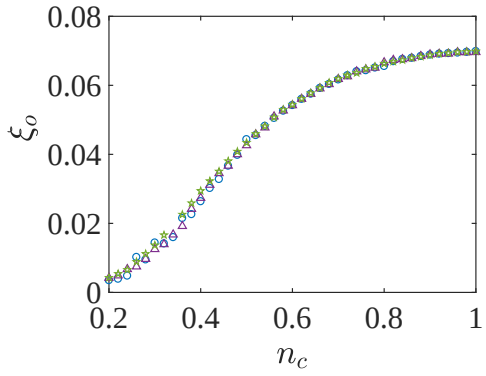

FIG. 3: (Color online) Variation of characteristic length ξ_0 as a function of the shear-thinning index n_c for different values of λ: $\lambda = 1(\star), \lambda = 10(\triangle), \lambda = 100(\circ)$.

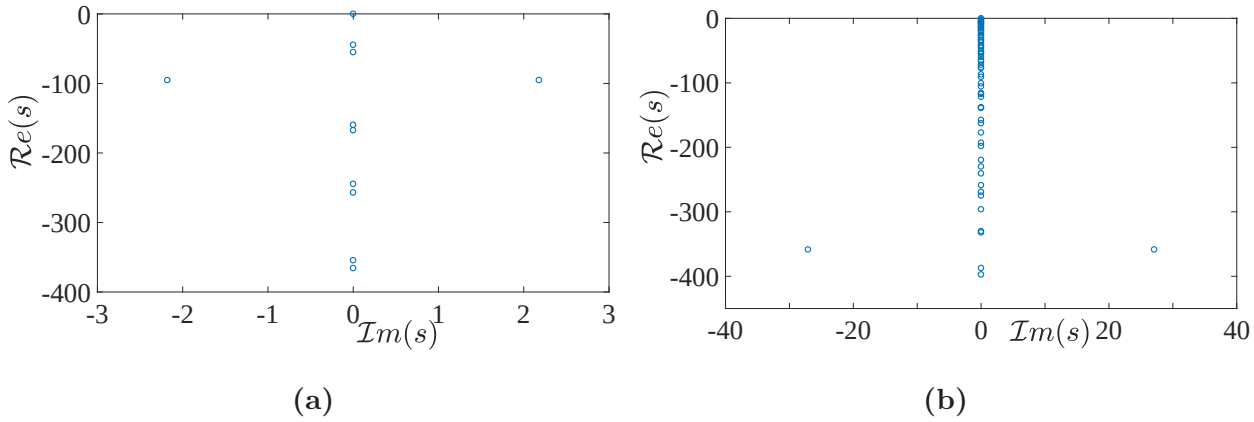

FIG. 4: (Color online) Eigenspectra for axisymmetric perturbations at critical conditions with $\eta = 0.4$. **(a)** Newtonian fluid at $\mathcal{R}_c = 68.296$, $k_c = 3.183$. **(b)** Carreau fluid with $n_c = 0.2$, $\lambda = 44$ at $\mathcal{R}_c = 2.282$, $k_c = 8.355$.

ing shear-thinning fluids among themselves and against Newtonian fluid can be radically different from one choice to another. The influence of the rheological parameters n_c and λ on the axial wave number and therefore on the size of the Taylor vortices is represented in figure 5(b). With increasing shear-thinning effects, the axial wavelength, $2\pi/k_c$ decreases significantly because of a strong viscosity stratification. As indicated in the analysis of the base flow, for weak values of n_c and large values of λ, a highly viscous fluid layer adjacent to the outer wall is formed.

The structure of the critical eigenfunctions is depicted in figure 6 for $\lambda = 44$ and different values of n_c. Here $V_{11}(r)$ is a real-valued function, whereas $F_{11}(r)$ is purely imaginary. With

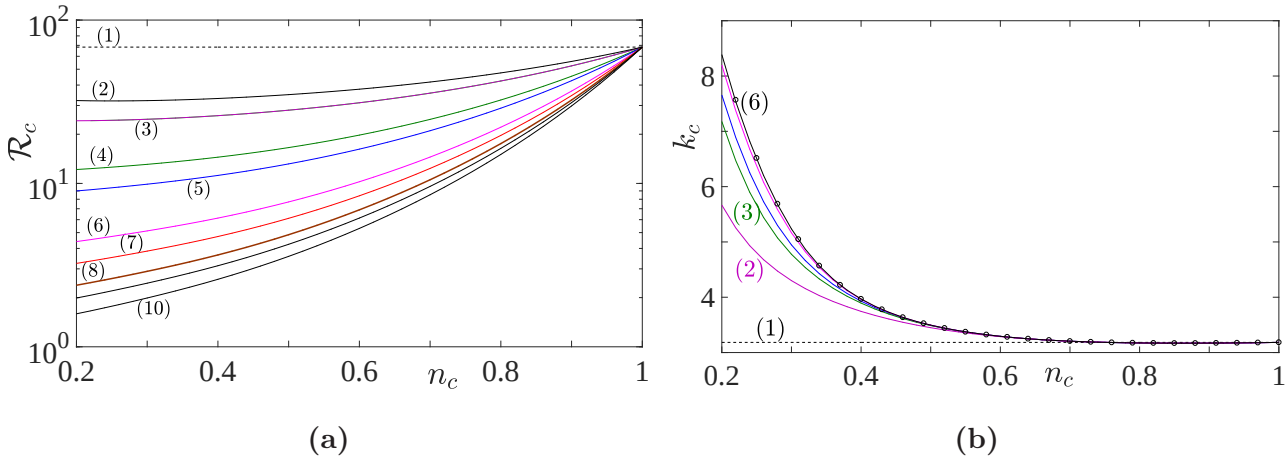

FIG. 5: (Color online) Carreau fluid. **(a)** Variation of the critical Reynolds number as function of shear-thinning index for different values of dimensionless constant time λ. (1) $\lambda = 0$ (Newtonian fluid); (2) $\lambda = 0.1$; (3) $\lambda = 0.2$; (4) $\lambda = 1$; (5) $\lambda = 2$; (6) $\lambda = 10$; (7) $\lambda = 20$; (8) $\lambda = 40$; (9) $\lambda = 60$; (10) $\lambda = 100$. **(b)** Variation of the critical axial wave-number as function of shear-thinning index for different values of λ. (1) $\lambda = 0$ (Newtonian fluid); (2) $\lambda = 0.2$; (3) $\lambda = 1$; (4) $\lambda = 2$; (5) $\lambda = 10$; (6) $\lambda = 100$. The symbol ($\circ$) corresponds to a power-law fluid.

increasing shear-thinning effects, variations of $F_{11}(r)$ and $V_{11}(r)$ are mainly confined in a thin layer adjacent to the inner cylinder where the viscosity is lower, and a large part of the annular space is unaffected by the perturbation: the vortices are squeezed against the inner wall. Furthermore, the eigenfunction and consequently the associated radial and axial velocity components are strongly reduced.

Remarks

- The validity of our program has been tested by comparing our results to the ones of Chandrasekhar [38] for a Newtonian fluid at different radius ratios η. A very good agreement is found as indicated by Tab. I (in Appendix A). For the Carreau model, the critical Reynolds number can be recalculated in terms of the inner wall shear viscosity and compared with the values given by Alibenyahia et al. [16]. Again, a very good agreement is found as shown by Tab. II (Appendix A).

- The bifurcation from a stationary circular Couette flow to a stationary Taylor vortex flow discussed above is not specific to Carreau model. Actually, the principle of exchange of stability holds for any purely viscous non-Newtonian fluid, where the instability of the

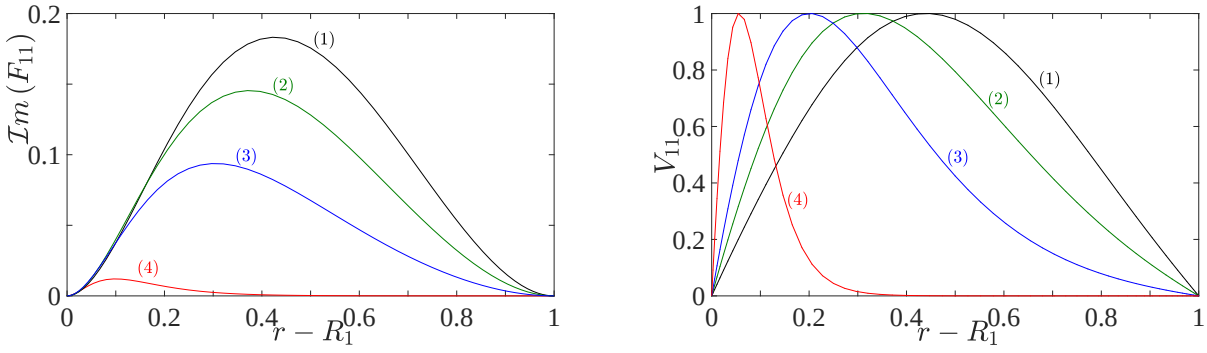

(a) **(b)**

FIG. 6: (Color online) Critical eigenfunctions at $\eta = 0.4$, for Carreau fluids with $\lambda = 44$ and different values of the shear-thinning index: (1) $n_c = 1$, $\mathcal{R}_c = 68.296$; (2) $n_c = 0.7$, $\mathcal{R}_c = 10.301$; (3) $n_c = 0.5$, $\mathcal{R}_c = 4.702$ and (4) $n_c = 0.2$, $\mathcal{R}_c = 2.282$.

circular Couette flow is inertial. Therefore, the oscillating mode observed for instance by Crumeyrolle *et al.* [39] at the onset for some polymer solutions which are viscoelastic and shear-thinning is a signature of the emergence of elastic effects.

III.1.1. Linear energy equation

The linear energy equation is derived by multiplying (41), (42) by r times the complex conjugate $(F_{11}^*, V_{11}^*)^T$ then integrating between the two cylinders. One obtains

$$\mathcal{R}e(s)\left\langle k^2|F_{11}|^2 + |V_{11}|^2 + |D_*F_{11}|^2\right\rangle = \mathcal{R}J_I - J_{\mu_b} + J_{\mu_b-\mu_t}, \tag{46}$$

where $\langle(.)\rangle = \displaystyle\int_{R_1}^{R_2}(.)r\,\mathrm{d}r$, J_I, J_{μ_b} and $J_{\mu_b-\mu_t}$ denote inertial and viscous contributions to the kinetic energy growth of the perturbation. They are defined by:

$$J_I = -\left\langle \dot{\gamma}^b_{r\theta}\left(-ik_cF_{11}\right)V_{11}^*\right\rangle, \tag{47}$$

$$J_{\mu_b} = \left\langle \mu_b\left[\frac{1}{2}\left(|\dot{\gamma}'_{\theta\theta}|^2 + |\dot{\gamma}'_{zz}|^2 + |\dot{\gamma}'_{rr}|^2\right) + |\dot{\gamma}'_{rz}|^2 + |\dot{\gamma}'_{r\theta}|^2 + |\dot{\gamma}'_{\theta z}|^2\right]\right\rangle, \tag{48}$$

$$J_{\mu_b-\mu_t} = \left\langle (\mu_b - \mu_t)\,|\dot{\gamma}'_{r\theta}|^2\right\rangle, \tag{49}$$

with $\dot{\gamma}'_{ij} = \dot{\gamma}_{ij}(\boldsymbol{u})$. At criticality, the transfer of energy from the base flow to the perturbation $\mathcal{R}\,J_I$ is exactly balanced by the viscous dissipation $(J_{\mu_b} - J_{\mu_b-\mu_t})$. The decrease of the critical Reynolds number with increasing shear-thinning effects means that

$$\mathcal{R}_c = \frac{J_{\mu_b} - J_{\mu_b-\mu_t}}{J_I} \tag{50}$$

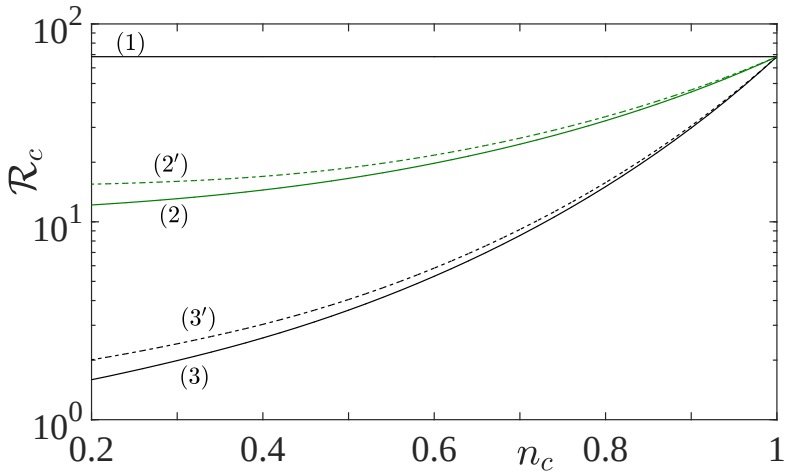

FIG. 7: (Color online) Critical Reynolds number as a function of the shear-thinning index for Carreau fluids at $\lambda = 1$, curves (2) and (2') and $\lambda = 100$, curve (3) and (3'). In the curves (2) and (3), the viscosity perturbation is taken into account. In the curves (2') and (3'), the viscosity perturbation is not taken into account. Curve (1) is represented as a reference and corresponds to the Newtonian case.

decreases with increasing shear-thinning effects. The term $J_{\mu_b-\mu_t}$ originates in the viscosity perturbation. It is positive definite and produces a reduction of the viscous dissipation and thus a decrease of the critical Reynolds number. This decrease is quite modest as it is shown by figure 7, where $\mathcal{R}_c$ is compared with that obtained when the viscosity perturbation is not taken into account.

The numerical results show that J_I and J_{μ_b} decrease with increasing shear-thinning effects. However, J_{μ_b} decrease faster than J_I. Thus $\mathcal{R}_c$ decreases with increasing shear-thinning effects. The integrand of J_I contains $\dot{\gamma}_{r\theta b}$ and the quadratic product of the eigenfunctions. The integrand of J_{μ_b} contains μ_b, the quadratic product of the eigenfunctions and their first derivatives. The eigenfunctions are normalized such that $max\,(V_{11}) = 1$.

The variations of J_I and J_{μ_b} with shear-thinning effects, has to be due to change with n_c (for instance), in either $\dot{\gamma}_{r\theta b}$, μ_b or the eigenfunctions.

Figure 10(a) shows that the integrand of J_{μ_b} decreases with increasing shear-thinning effects. Figure 10(b) shows that the eigenfunctions contribute to increase the viscous dissipation. Therefore the decrease of J_{μ_b} is due to μ_b.

Analysis of figures 9(a) and 10(a), show that the eigenfunctions contribute to a decrease of J_I. The shear rate $\dot{\gamma}_{r\theta b}$ attenuates this decrease and amplifies the transfer of energy from the

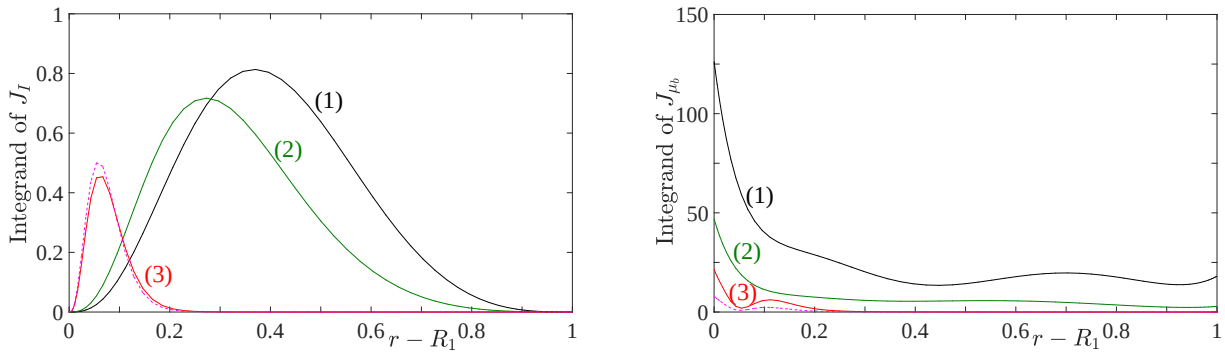

(a) **(b)**

FIG. 8: (Color online) Integrands of J_I **(a)** and J_{μ_b} **(b)** at critical conditions: (1) Newtonian fluid; (2) Carreau fluid with $n_c = 0.7, \lambda = 1$; (3) Carreau fluid with $n_c = 0.2$, $\lambda = 1$; (4 dashed line) Carreau fluid with $n_c = 0.2, \lambda = 10$.

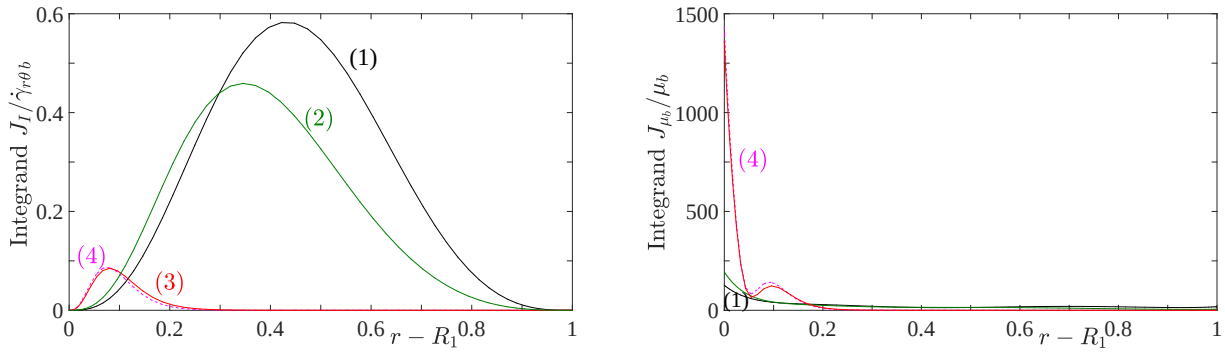

(a) **(b)**

FIG. 9: (Color online) Integrands of $J_I/\dot{\gamma}_{r\theta b}$ **(a)** and J_{μ_b}/μ_b **(b)** at critical conditions: (1) Newtonian fluid; (2) Carreau fluid with $n_c = 0.7, \lambda = 1$; (3) Carreau fluid with $n_c = 0.2$, $\lambda = 1$; (4 dashed line) Carreau fluid with $n_c = 0.2, \lambda = 10$.

base flow to perturbation. Consequently, it appears that changes in the eigenfunctions with shear-thinning effects cannot be responsible for the decrease of $\mathcal{R}_c$ and the effect has to be due to the change in the base flow: increase of the shear-rate and decrease of the viscosity near the inner wall.

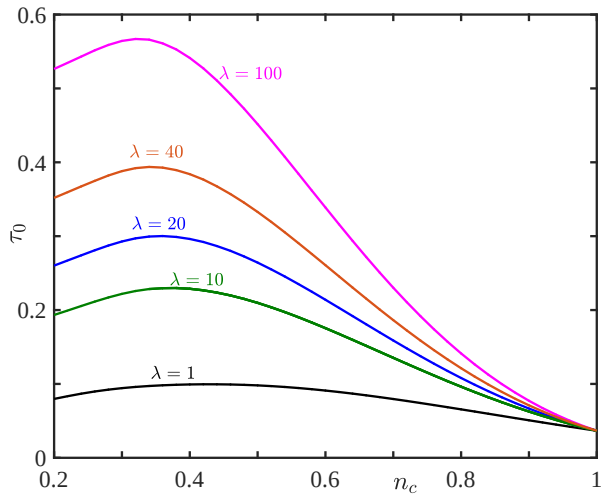

FIG. 10: (Color online) Variation of the characteristic time of circular Couette flow instability as function of the shear-thinning index for different values of the dimensionless constant-time of the fluid. The radius ratio is $\eta = 0.4$.

III.2. Characteristic time

In the neighborhood of the critical conditions such that $(\mathcal{R} - \mathcal{R}_c)/\mathcal{R}_c = \epsilon << 1$, the growth rate can be approximated using Taylor expansion

$$s = \frac{\epsilon}{\tau_0} + O\left(\epsilon^2\right), \tag{51}$$

where τ_0 is the characteristic time for the instability to grow. The determination of τ_0 can be obtained by evaluating $\left(\frac{ds}{d\epsilon}\right)_{\epsilon=0}$ (s is calculated for different values of ϵ, around $\epsilon = 0$). Figure 10 shows for a Carreau fluid, the variation of τ_0 as a function of the shear-thinning index n_c for different values of λ. The characteristic time for the instability to grow increases significantly with λ, reaches a maximum at $n_c \approx 0.3$ then decreases slightly as n_c decreases. These results reveal that the onset of Taylor vortex flow is much more gradual for a shear-thinning fluid than for a Newtonian fluid.

III.3. Adjoint mode

To the direct problem (44) is associated the adjoint problem

$$s\boldsymbol{M}^+ \cdot \boldsymbol{X}_{ad} = \boldsymbol{L}^+ \cdot \boldsymbol{X}_{ad} \quad \text{with} \quad \boldsymbol{X}_{ad} = (F_{ad}, V_{ad}) \ . \tag{52}$$

The adjoint operators $\boldsymbol{M}^+$ and $\boldsymbol{L}^+$ are defined by

$$\langle \boldsymbol{X}_{ad}, \boldsymbol{M}\cdot\boldsymbol{X}\rangle = \langle \boldsymbol{M}^+\cdot\boldsymbol{X}_{ad}, \boldsymbol{X}\rangle \quad \text{and} \quad \langle \boldsymbol{X}_{ad}, \boldsymbol{L}\cdot\boldsymbol{X}\rangle = \langle \boldsymbol{L}^+\cdot\boldsymbol{X}_{ad}, \boldsymbol{X}\rangle\,, \tag{53}$$

with the inner product between two vector functions $\boldsymbol{f}(r)$ and $\boldsymbol{g}(r)$,

$$\langle \boldsymbol{f}, \boldsymbol{g}\rangle = \int_{R_1}^{R_2} \boldsymbol{f}^*\cdot\boldsymbol{g}\, r\, dr\,, \tag{54}$$

where f^* is the complex conjugate of f. The adjoint problem associated to (41), (42) is

$$s\left(DD_* - k^2\right)F_{ad} = ik\mathcal{R}\frac{V_b}{r}V_{ad} + \left(DD_* - k^2\right)\left[\mu_b\left(DD_* - k^2\right)F_{ad}\right] + 2k^2\left(D^2\mu_b\right)F_{ad}\,, \tag{55}$$

$$sV_{ad} = -2ik\mathcal{R}\left(D_*V_b\right)F_{ad} + \frac{1}{r^2}D\left[r^2\mu_t\left(DV_{ad} - \frac{V_{ad}}{r}\right)\right] - k^2\mu_b V_{ad}\,, \tag{56}$$

with

$$F_{ad} = DF_{ad} = V_{ad} = 0 \quad \text{at} \quad r = R_1, R_2. \tag{57}$$

IV. WEAKLY NONLINEAR STABILITY ANALYSIS

IV.1. Principle and formulation

A weakly nonlinear analysis using the amplitude expansion method is used as a first approach to investigate nonlinear effects. Near the bifurcation point, the dynamics are assumed to be determined by the fundamental mode with wavenumber $k = k_c$, its higher harmonics generated by the the nonlinear self-interactions and the modification of the base state due to the interactions with the complex conjugate. It is natural to write the nonlinear perturbation as the Fourier series

$$\left[\phi\left(r,z,t\right),\, v\left(r,z,t\right)\right] = \sum_{n=-\infty}^{+\infty}\left[\phi_n\left(r,t\right), v_n\left(r,t\right)\right]E^n \quad \mathsf{with} \quad E^n = e^{ink_cz}. \tag{58}$$

The transient evolution of the perturbation is taken into account by the temporal evolution of the Fourier coefficients ϕ_n and v_n. Because ϕ and v are real, we have $\phi_{-n} = \phi_n^*$ and $v_{-n} = v_n^*$, where the star denotes the complex conjugate. Substituting (58) into (36) and (37) and separating out the coefficients of similar exponentials, we obtain a set of nonlinear partial differential equations for the Fourier components ϕ_n and v_n:

$$\frac{\partial}{\partial t}\mathcal{S}_n\phi_n = \mathcal{S}_n\left[\mathcal{S}_n\left(\mu_b\phi_n\right)\right] - 2ink\mathcal{R}e\frac{V_b}{r}v_n + \left[NI1\right]_{E^n} + \left[NV1\right]_{E^n}\,, \tag{59}$$

$$\frac{\partial}{\partial t}v_n = ink_c\mathcal{R}e\left(D_*V_b\right)\phi_n + \frac{1}{r^2}D\left[r^2\mu_t\left(Dv_n - v_n/r\right)\right] + \left[NI2\right]_{E^n} + \left[NV2\right]_{E^n}\,, \tag{60}$$

with

$$\mathcal{S}_n = DD_* - n^2 k_c^2, \tag{61}$$

$[NI]_{E^n}$ and $[NV]_{E^n}$ the coefficients of E^n in the nonlinear inertial and nonlinear viscous terms respectively. The nonlinear viscous terms arise from the shear-thinning behavior. As in references [25–28, 40, 41], the amplitude $A(t)$ of the fundamental mode (ϕ_1, v_1) is considered as small, therefore the Fourier components ϕ_n and v_n can be sought using a perturbation method expanding around the solution of the linear problem:

$$[\phi_1(r,t), v_1(r,t)] = A(t)\,[F_1(r,t), V_1(r,t)]\ . \tag{62}$$

The amplitude of the perturbation is defined by setting

$$A(t) = max(v_1(r,t))\,. \tag{63}$$

It is clear that if the linear solution is $O(A)$, the leading term of (ϕ_2, v_2) is $O(A^2)$ because of the interaction of the fundamental with itself. The same reasoning applied to higher harmonics shows that (ϕ_n, v_n) can be written as

$$[\phi_n(r,t), v_n(r,t)] = A^n(t)\,[F_n(r,t), V_n(r,t)] \quad \text{if} \quad n > 0, \tag{64}$$

and

$$[\phi_0(r,t), v_0(r,t)] = A^2(t)\,[F_0(r,t), V_0(r,t)]\ . \tag{65}$$

Substituting (64) and (65) into (59) and (60) and equating similar powers of $A(t)$, leads to the following set of equations for F_n and V_n

$$\left(\frac{\partial}{\partial t} + ng\right)\mathcal{S}_n F_n = \mathcal{S}_n\left[\mathcal{S}_n\left(\mu_b F_n\right)\right] - 2inkRe\frac{V_b}{r}V_n + [NI1]_{A^nE^n} + [NV1]_{A^nE^n}\,, \tag{66}$$

$$\left(\frac{\partial}{\partial t} + ng\right)V_n = ink_cRe\left(D_*V_b\right)F_n + \frac{1}{r^2}D\left[r^2\mu_t\left(DV_n - V_n/r\right)\right] + [NI2]_{A^nE^n} + [NV2]_{A^nE^n}\,. \tag{67}$$

The time evolution of the amplitude $A(t)$ is given by the Stuart-Landau equation

$$g = \frac{1}{A}\frac{dA}{dt} = \sum_{m=0} g_m\,|A|^{2m}\ , \tag{68}$$

where $g_0 = s$ is the linear eigenvalue, and g_m with $m > 1$, the mth Landau coefficient. Since $F_n(V_n)$ is $O(1)$ or $O(A^2)$ as $A \to 0$, the nonlinearities generate terms in ascending power of A^2. Hence, F_n and V_n are expanded as follows

$$F_n(r,t) = \sum_{m=0}^{+\infty} F_{n,2m+n}(r)A^{2m}\ , \quad V_n(r,t) = \sum_{m=0}^{+\infty} V_{n,2m+n}(r)A^{2m}. \tag{69}$$

Substituting (69) into (66) and (67) and using (68) yields the differential equations for $F_{n,2m+n}$ and $V_{n,2m+n}$,

$$L1_{nm}F_{n,2m+n} + L2_{nm}V_{n,2m+n} = [NI1]_{E^nA^{2m+n}} + [NV1]_{E^nA^{2m+n}} - \sum_{j=1}^{m} [2(m-j)+n]\, g_j \mathcal{S}_n F_{n,2(m-j)+n} \tag{70}$$

$$L3_{nm}F_{n,2m+N} + L4_{nm}V_{n,2m+n} = [NI2]_{E^nA^{2m+n}} + [NV2]_{E^nA^{2m+n}} - \sum_{j=1}^{m} [2(m-j)+n]\, g_j V_{n,2(m-j)+n}\,, \tag{71}$$

with

$$L1_{nm} = (2m+n)\, s\mathcal{S}_n - \mathcal{S}_n\,(\mu_b \mathcal{S}_n) \quad , \quad L2_{nm} = -2ink_c\mathcal{R}V_b/r\,, \tag{72}$$

$$L3_{nm} = -ink_c\mathcal{R}\,(D_*V_b) \quad , \quad L4_{nm} = (2m+n)\, s - \frac{1}{r^2}D\left[r^2\mu_t\,(D-1/r)\right] \tag{73}$$

IV.2. Solution procedure

The system of differential equations (70) and (71) is solved sequentially beginning from $n = 1$ and $m = 0$. The problem $n = 1$, $m = 0$ is the linear problem (41) and (42). The problem $n = 0, m = 1$ yields the first correction to the base flow, the problem $n = 2$, $m = 0$ yields the second harmonic mode; $n = 1$, $m = 1$ yield the coefficient g_1 of feedback on the fundamental mode. More precisely, g_1 is determined using the solvability condition to the equation which gives the modification of the fundamental mode. For each (n, m), the system of differential equations (70), (71) with the associated boundary conditions is solved numerically using a spectral collocation method based on Chebyshev polynomials as in the linear problem (41)-(43).

V. RESULTS AND DISCUSSION

V.1. Modification of the base flow

The interaction of the fundamental AF_{11}, AV_{11} with its complex conjugate through the nonlinear quadratic terms produces a correction of the basis state: A^2F_{02} and A^2V_{02}. Equations for F_{02} and V_{02} are obtained by setting $n = 0$ and $m = 1$ in (70)-(73). The factor of A^2E^0 arising from the nonlinear inertial and nonlinear viscous terms in (70) vanish, therefore

$$F_{02} = 0\,. \tag{74}$$

The modification of the base flow satisfies the following equation

$$\frac{1}{r^2}D\left[r^3\mu_t D\left(\frac{V_{02}}{r}\right)-2sV_{02}\right]=-\mathcal{R}\left(\frac{\partial\phi}{\partial z}D_*v-D_*\phi\frac{\partial v}{\partial z}\right)_{A^2E^0} -\frac{1}{r^2}D\left(r^2\tau_{2,r\theta}\right)_{A^2E^0}, \tag{75}$$

with the boundary conditions

$$V_{02}=0 \quad \text{at} \quad r=R_1,R_2\,. \tag{76}$$

In equation (75), $(\cdot)_{A^2E^0}$ means the coefficient of A^2E^0 in the nonlinear inertial or nonlinear viscous terms. Figure 11 shows the modification of the base flow at order A^2 for $\lambda=1$ and different values of n_c. One notes that with increasing shear-thinning effects (decreasing n_c), $V_{02}(r)$ becomes more concentrated in the neighborhood of the inner cylinder because of the viscosity stratification. Furthermore, the numerical results indicate that from $\lambda=1$, there is practically no influence of this parameter.

The profiles of V_{02} are related to the radial inflow and outflow jets. The radial inflow jet carries fluid particles with low azimuthal momentum from the outer cylinder inward, decreasing the azimuthal velocity near the inner cylinder. The radial outflow jet carries fluid particles with high azimuthal momentum from the inner cylinder outward, increasing the azimuthal velocity near the outer cylinder. This reorganization of the azimuthal flow tends to increase $|dV/dr|$ at the walls and to reduce $|dV/dr|$ in the fluid interior. Note also that the deficit of the azimuthal velocity near the inner cylinder is higher than the surplus near the outer cylinder. Canceling artificially, the nonlinear viscous terms in (75) allows to highlight the contribution of the nonlinear inertial terms and vice-versa, to highlight the contribution of the nonlinear viscous terms on the modification of the base flow.

The contribution of the nonlinear viscous terms, which arise from the viscosity perturbation is shown in Fig. 12(a). The azimuthal velocity is increased in practically all the annular space, and mainly near the inner cylinder for strong shear-thinning effects. This is a consequence of the reduction of the viscous dissipation described by the term $J_{\mu_b-\mu_t}$ in equation (49). The modification of the base flow by the nonlinear viscous terms is weaker, but of the same magnitude order, than that induced by the nonlinear inertial terms shown in figure 12(b). The difference between these two contributions decreases with increasing shear-thinning effects.

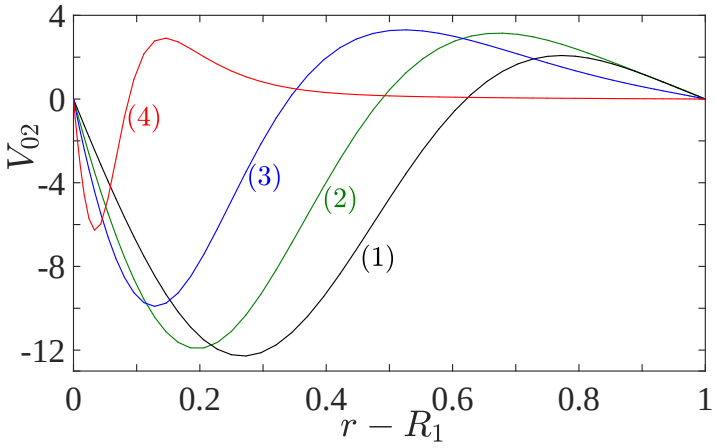

FIG. 11: (Color online) Modification of the base flow at $\eta = 0.4$, for Carreau fluids with $\lambda = 1$ and different values of the shear-thinning index: (1) $n_c = 1$ Newtonian fluid; (2) $n_c = 0.7$; (3) $n_c = 0.5$ and (4) $n_c = 0.2$.

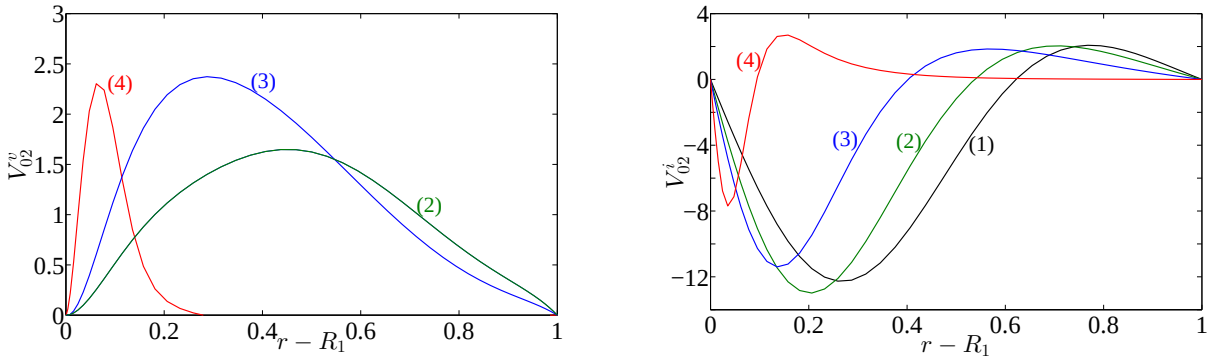

(a) **(b)**

FIG. 12: (Color online) Modification of the base flow at $\eta = 0.4$, for Carreau fluids with $\lambda = 100$ and different values of the shear-thinning index: (1) $n_c = 1$; (2) $n_c = 0.7$; (3) $n_c = 0.5$ and (4) $n_c = 0.2$. **(a)** Contribution of nonlinear viscous terms; **(b)** contribution of nonlinear inertial terms.

V.2. Second harmonic mode

Interaction of the fundamental (AF_{11}, AV_{11}) with itself through the quadratic nonlinear terms in the perturbations equations (36), (37) generates the second harmonic, $A^2\,(F_{22}, V_{22})$. Equations for F_{22} and V_{22} are obtained by setting $n = 2$, $m = 0$ in (70) and (71) and extracting the factors of A^2E^2 in the nonlinear terms. At order $n = 2$, $m = 0$, equations

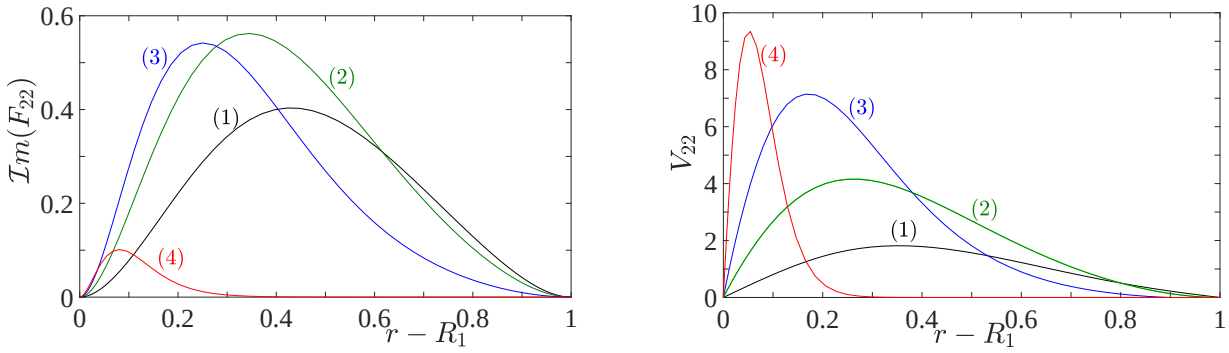

(a) **(b)**

FIG. 13: (Color online) Second harmonic mode at the critical conditions for $\eta = 0.4$, $\lambda = 10$ and different values of the shear-thinning index: (1) $n_c = 1$ Newtonian case; (2) $n_c = 0.7$; (3) $n_c = 0.5$; (4) $n_c = 0.2$. **(a)** Radial profile of $\mathcal{I}m(F_{22})$; **(b)** azimuthal velocity V_{22}.

(70) and (71) reduce to

$$L1_{22}F_{22} + L2_{22}V_{22} = [NI1]_{A^2E2} + [NV1]_{A^2E^2}\,, \tag{77}$$

$$L3_{22}F_{22} + L4_{22}V_{22} = [NI2]_{A^2E2} + [NV2]_{A^2E^2}\,,. \tag{78}$$

The boundary conditions read

$$F_{22} = DF_{22} = V_{22} = 0 \quad \text{at} \quad r = R_1, R_2\,. \tag{79}$$

Radial profiles of $\mathcal{I}m(F_{22})$ and V_{22} are shown in figure 13 for $\lambda = 10$ and different values of n_c. As for the fundamental mode, with increasing shear-thinning effects, the variations of F_{22} and V_{22} are confined in a thin layer adjacent to the inner wall, i.e the second harmonic is squeezed against the inner cylinder. Furthermore, with increasing shear-thinning effects the maximum of the azimuthal velocity V_{22} is amplified, whereas the radial velocity is reduced.

V.3. Modification of the fundamental mode at cubic order: Cubic Landau constant

The nonlinear interactions between the fundamental, the second harmonic and the modification of the base flow lead to a cubic correction $O\left(A^3\right)$ to the fundamental mode. The first Landau coefficient g_1 accounts for these nonlinear interactions on the fundamental mode.

The modification of the fundamental mode at order A^3 is governed by (70) and (71) with $m = n = 1$, i.e.

$$L1_{13}F_{13} + L2_{13}V_{13} = [NI1]_{A^3E^1} + [NV1]_{A^3E^1} - g_1\mathcal{S}_1\, F_{11}\,, \tag{80}$$

$$L3_{13}F_{13} + L4_{13}V_{13} = [NI2]_{A^3E_1} + [NV2]_{A^3E^1} - g_1 V_{11}\,. \tag{81}$$

The boundary conditions are

$$F_{13} = DF_{13} = V_{13} = 0 \quad \text{at} \quad r = R_1, R_2\,. \tag{82}$$

The system (80) and (81) can be written

$$\boldsymbol{L}\cdot\boldsymbol{X}_{13} = -g_1\boldsymbol{M}\cdot\boldsymbol{X}_{11} + \boldsymbol{NI} + \boldsymbol{NV} \quad \text{with} \quad \boldsymbol{X}_{13} = (F_{13}, V_{13})\,. \tag{83}$$

At the critical conditions, (83) has a non-trivial solution if the Fredholm solvability condition is satisfied, i.e. orthogonality of the inhomogeneous part of (83) to the null-space of the adjoint operator of $\boldsymbol{L}$. The cubic Landau constant is then readily obtained,

$$g_1 = g_1^I + g_1^V = \left(g_{10}^I + g_{12}^I\right) + \left(g_{10}^V + g_{12}^V + g_{1-11}^V\right)\,, \tag{84}$$

with

$$g_{10}^I = \frac{\langle \boldsymbol{NI}\left(\boldsymbol{X}_{02}|\boldsymbol{X}_{11}\right), \boldsymbol{X}_{ad}\rangle}{\langle \boldsymbol{M}\cdot\boldsymbol{X}_{11}, \boldsymbol{X}_{ad}\rangle} \quad , \quad g_{10}^V = \frac{\langle \boldsymbol{NV}\left(\boldsymbol{X}_{02}|\boldsymbol{X}_{11}\right), \boldsymbol{X}_{ad}\rangle}{\langle \boldsymbol{M}\cdot\boldsymbol{X}_{11}, \boldsymbol{X}_{ad}\rangle} \tag{85}$$

$$g_{12}^I = \frac{\langle \boldsymbol{NI}\left(\boldsymbol{X}_{22}|\boldsymbol{X}_{-11}\right), \boldsymbol{X}_{ad}\rangle}{\langle \boldsymbol{M}\cdot\boldsymbol{X}_{11}, \boldsymbol{X}_{ad}\rangle} \quad , \quad g_{12}^V = \frac{\langle \boldsymbol{NV}\left(\boldsymbol{X}_{12}|\boldsymbol{X}_{-11}\right), \boldsymbol{X}_{ad}\rangle}{\langle \boldsymbol{M}\cdot\boldsymbol{X}_{11}, \boldsymbol{X}_{ad}\rangle} \tag{86}$$

$$g_{1-11}^V = \frac{\langle \boldsymbol{NV}\left(\boldsymbol{X}_{11}, \boldsymbol{X}_{11}|\boldsymbol{X}_{-11}\right), \boldsymbol{X}_{ad}\rangle}{\langle \boldsymbol{M}\cdot\boldsymbol{X}_{11}, \boldsymbol{X}_{ad}\rangle}\,, \tag{87}$$

where $\boldsymbol{X}_{-11} = \boldsymbol{X}_{11}^*$, g_{10}^I and g_{10}^V are the feedback of the mean flow correction onto the fundamental through the nonlinear inertial and nonlinear viscous terms respectively, g_{12}^I is the feedback of the second harmonic onto the fundamental, etc. The vertical bar notation in (85)-(87) may be better defined through an example of a nonlinear term. For instance $\left(D_*\phi\dfrac{\partial v}{\partial z}\right)(\boldsymbol{X_{22}}|\boldsymbol{X_{-11}}) \rightarrow D_*F_{22}(-ikV_{11}^*) + D_*F_{11}^*(2ikV_{22})$. The integrals in (85)-(87) are evaluated by means of the Clenshaw and Curtis method. In figure 14(a), g_1 is plotted as a function of n_c for different values of λ. The sign of g_1 is negative indicating a supercritical nature of the bifurcation. As expected for weakly shear-thinning effects, the contribution of the nonlinear viscous terms g_1^V, on the first Landau coefficient, play a minor role and $\left|g_1^I\right| >> g_1^V$. With increasing the shear-thinning effects (decreasing n_c), the contribution of

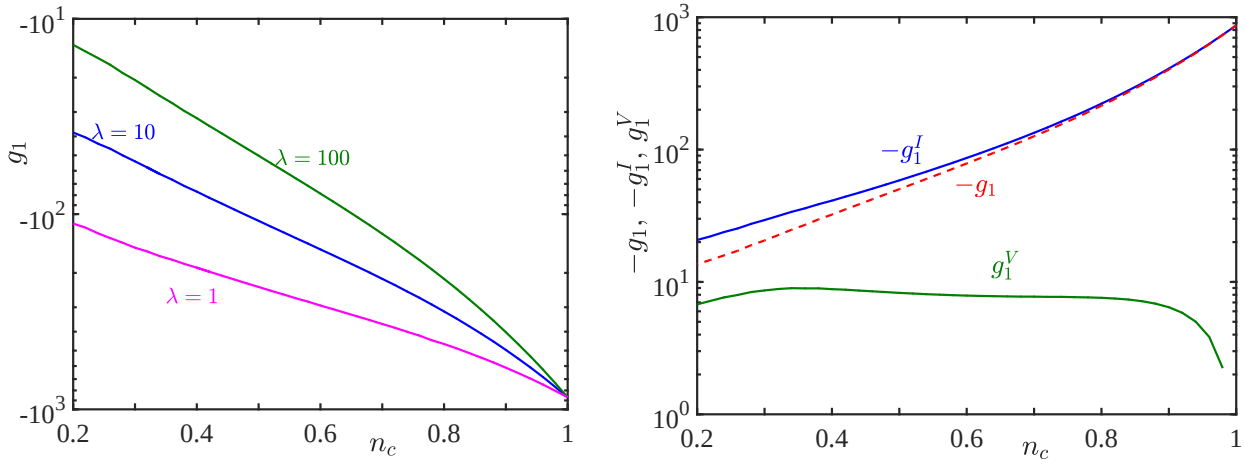

FIG. 14: (Color online) **(a)** Cubic Landau constant, g_1, as a function of n_c for different values of the dimensionless constant time λ with $\eta = 0.4$. **(b)** Contribution of the nonlinear inertial terms $(-g_1^I)$ and nonlinear viscous terms g_1^V at $\lambda = 100$.

the nonlinear inertial terms g_1^I and nonlinear viscous terms g_1^V become of the same order, however $|g_1^I|$ remains larger than g_1^V, as shown in figure 14(b). Note that g_1^V is positive, i.e. nonlinear viscous terms favor a subcritical bifurcation. Contributions of the different terms g_{10}^I, g_{12}^I, g_{12}^V ... that control the value of g_1 are given in Appendix B. The data show that for a Newtonian fluid, g_1 is dominated by the feedback of the base flow correction onto the fundamental. With increasing shear-thinning effects, the feedback of the second harmonic becomes more significant.

V.4. Features of the perturbation near the threshold

Besides the Landau coefficient, the amplitude of the perturbation A is an important quantity in the nonlinear stability analysis. It is obtained by setting $dA/dt = 0$ in (68). In the neighbourhood of the critical conditions, to lowest order in ϵ, the amplitude is

$$A = \sqrt{\frac{-\epsilon}{\tau_0\, g_1}}\,. \tag{88}$$

The numerical values of the Landau coefficient and hence the values the perturbation amplitude A depend upon the normalization condition used for the eigenfunction in the linear theory. However, the physical velocity components, i.e. the product of the amplitude with

the eigenfunctions of the linear theory are independent of the normalization. For instance, we can consider the mean kinetic energy of the perturbation or the torque applied on the inner cylinder.

V.4.1. Mean kinetic energy

At order A^2, the mean kinetic energy is defined by

$$\xi = A^2 \int_{R_1}^{R_2} \left(k_c^2 \left| F_{11} \right|^2 + \left| V_{11} \right|^2 + \left| D_* F_{11} \right|^2 \right) r \mathrm{d}r \,. \tag{89}$$

Figure 15(a) plots ξ as a function of ϵ for different values of the shear-thinning index n_c. The dimensionless constant time is fixed $\lambda = 10$. The curves are practically identically to those obtained for a power-law fluid. As it can be observed the kinetic energy of the perturbation decreases with increasing shear-thinning effects. Figure 15(b) shows that the azimuthal kinetic energy is much larger than the radial and axial ones. For instance at $n_c = 0.2$, more than 95% of the kinetic energy is concentrated on the azimuthal velocity.
The decrease of the kinetic energy with increasing shear-thinning effects is due to the viscosity stratification. Indeed, with increasing shear-thinning effects, the Taylor vortices are confined in the thin region near the inner wall where the viscosity is low (the perturbations are suppressed in the highly viscous fluid at a short distance from the inner cylinder) and their strength becomes weaker as shown in figure 6a.

V.4.2. Torque

The determination of the torque $\hat{T}$ applied on the inner cylinder is of great interest. It provides information about the energy dissipation since the energy injected in the fluid per unit of time is obtained by multiplying the torque by the velocity of the inner cylinder. Dubrulle [42] and Eckhardt [43] demonstrated that the dimensionless torque $G = \hat{T}/2\pi\hat{\rho}\hat{\nu}^2\hat{h}$ where $\hat{\nu}$ is the kinematic viscosity and $\hat{h}$ the height of the inner cylinder, is related to the angular momentum flux. By analogy with the heat transfer in Rayleigh-Bénard convection, the previous authors defined a pseudo-Nusselt number, Nu_* for a Taylor Couette flow as the ratio of G to the dimensionless torque of the laminar flow G_b. Hence, for a purely viscous fluid,

$$Nu_* = \frac{G}{G_b} = \frac{\int_0^{2\pi/k_c} \left(\mu \dot{\gamma}_{r\theta} \right)_{r=R_1} \mathrm{d}z}{\left(2\pi/k_c \right) \left(\mu_b \dot{\gamma}_{r\theta b} \right)_{r=R_1}} \,. \tag{90}$$

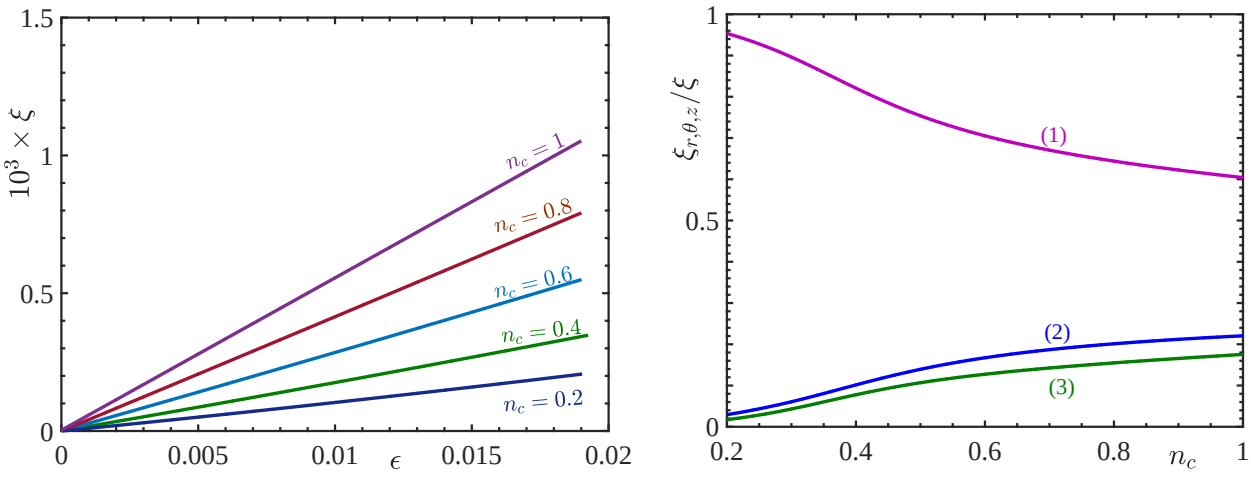

(a) **(b)**

FIG. 15: (Color online) **(a)** Kinetic energy at order A^2 for different values of the shear-thinning index n_c with $\lambda = 10$ and $\eta = 0.4$. **(b)** Ratio of azimuthal ξ_θ (curve 1), radial ξ_r (curve 2) and axial ξ_z (curve 3) kinetic energy to the total kinetic energy ξ.

Using (17) and (28)-(33), Nu_* can be written as

$$Nu_* = 1 + \left(\frac{\mu_t}{\mu_b}\right)_{R_1} \frac{\int_0^{2\pi/k_c} \left(\dot{\gamma}_{r\theta}\right)_{r=R_1} \mathrm{d}z}{\left(\dot{\gamma}_{r\theta b}\right)_{r=R_1}} + \frac{\int_0^{2\pi/k_c} \left(\mu_1 \dot{\gamma}_{r\theta} + \mu_2 \dot{\gamma}_{r\theta b}\right)_{r=R_1} \mathrm{d}z}{\left(\mu_b \dot{\gamma}_{r\theta b}\right)_{r=R_1}} + \ldots \tag{91}$$

In the laminar regime, the angular momentum flux is diffusive and $Nu_* = 1$. In the TVF regime, the pseudo-Nusselt number at order A^2 is given by

$$Nu_* = 1 + A^2 \left(\frac{\mu_t}{\mu_b}\right)_{R_1} \left(\frac{DV_{02}}{DV_b}\right)_{R_1} + 2\frac{A^2}{\left(\mu_b\right)_{r=R_1}} \left(\frac{\mathrm{d}\mu_b}{\mathrm{d}\Gamma_b}\right)_{R_1} \left(3\left|DV_{11}\right|^2 + \left|D^2 F_{11}\right|^2\right)_{R_1} + 4\frac{A^2}{\left(\mu_b\right)_{r=R_1}} \left(\frac{\mathrm{d}^2\mu_b}{\mathrm{d}\Gamma_b^2}\right)_{R_1} \left|DV_{11}\right|^2_{R_1} + O\left(A^4\right) . \tag{92}$$

Using (88), the pseudo-Nusselt number can be written formally as

$$Nu_* = 1 + K\epsilon\,. \tag{93}$$

For a Newtonian fluid, the expression of the slope K reduces to

$$K = -\frac{1}{\tau_0 g_1} \frac{\left(DV_{02}\right)_{R_1}}{\left(DV_b\right)_{R_1}} \quad \text{with} \quad DV_b = -\frac{2}{\eta\left(1+\eta\right)} \tag{94}$$

In this case, the increase of the torque applied on the inner cylinder is due to the increase of the inner wall shear rate of the mean flow, via the term $\left(DV_{02}\right)_{R_1}$. For non-Newtonian shear-thinning fluids, there is an additional term arising from the viscosity perturbation

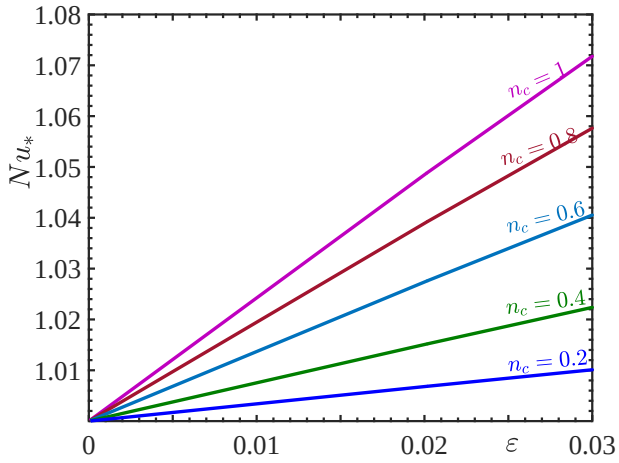

FIG. 16: (Color online) Torque applied on the inner cylinder, at order A^2, versus ϵ for different values of the shear-thinning index n_c with $\lambda = 10$.

as indicated by (92). Figure 16 shows the variation of Nu_* with ϵ, for different values of n_c. The dimensionless constant time of the fluid is fixed at $\lambda = 10$. The pseudo-Nusselt number decreases with increasing shear-thinning effects, in agreement with the decrease of the kinetic energy of the perturbation. The intensity of the Taylor vortices diminishes and thus the modification of the shear-rate at the inner wall is weaker. However, the analysis of the different terms in equation (91) shows that for a strong shear-thinning fluid, the term $\mu_1 \dot{\gamma}_{r\theta}(\boldsymbol{u})$ plays a significant role in the reduction of Nu_*. This term called "non-Newtonian Reynolds-stress" in [44] contributes to the reduction of the viscous dissipation.

V.5. Validation by computing higher-order Landau constants

Figures 15 and 16 indicate that the kinetic energy of the perturbation and the pseudo-Nusselt number Nu_* decrease with increasing shear-thinning effects. This result was obtained by truncating the series (68) to the first Landau constant, at cubic order in A. For a significant deviation from the critical condition, terms of higher order become large and should be taken into account. A weakly nonlinear expansion was then carried out up to seventh-order in amplitude. As in the Newtonian case, for shear-thinning fluids, the Landau constants are of the same sign and increase very fast, i.e. A has to be very small to satisfy the assumption of the weakly nonlinearity. This increase is stronger with increasing shear-thinning effects as it is shown by the data in table V (Appendix C). The representation

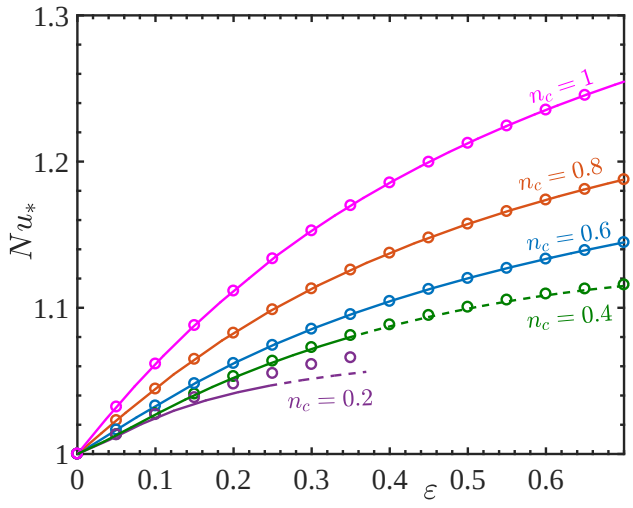

FIG. 17: (Color online) Influence of shear thinning effects on the pseudo-Nusselt number at $\eta = 0.4$ and $\lambda = 10$. The symbols correspond to a power-law model for the same shear-thinning index.

of the equilibrium amplitude versus ϵ at figure 27 (Appendix C), at the third-, fifth- and seventh-order shows that the correction brought by adding a new term decreases.

Figure 17 shows the variation of the pseudo-Nusselt number as a function of ϵ for different values of n_c. As it can be observed, the decrease of Nu_* with increasing shear-thinning effects is confirmed at least for a reasonable distance from the critical conditions. Curves for Carreau and power-law models are not distinguishable except for $n_c = 0.2$. In this last case, a higher value of λ is needed.

Similarly, the numerical results show that for a reasonable departure from the critical conditions, the kinetic energy of the perturbation decreases with increasing shear-thinning effects and it is mainly concentrated on the azimuthal velocity component.

Remarks

- Our results for $Nu*$ are compared with those obtained experimentally by Donnelly & Simon [45] for a Newtonian fluid with $\eta = 0.5$. A good agreement is found at least up to $\epsilon = 0.5$ as it is illustrated by Tab. III (Appendix A). With the exception of one point, the relative difference is less than 1 %.

- For $n_c = 0.2$ and 0.4, the curves Nu_* versus ϵ are dashed when ϵ exceeds a particular value say ϵ_0. Actually, harmonics analysis done in §V.7 shows that for sufficiently strong shear-thinning effects, the fourth harmonic overtakes the third one when $\epsilon > \epsilon_0$, which may

delimit the range of validity of the results.
- Departing sufficiently from the critical conditions, we can no longer assume $s = 0$ in the equations that describe the modification of the fundamental mode. Hence, these equations become unconditionally solvable. To calculate the Landau coefficients, an iterative process was used as suggested by Sen & Venkateswarlu [28] (See also Bouteraa et al. [46] and Bouteraa & Nouar [47]).

V.6. Description of the flow field

The change in the flow structure with increasing shear-thinning effects is described by contours of stream function ψ, azimuthal vorticity and velocity components u, v and w. Figure 18 shows isolines of constant ψ on one wavelength $\lambda_z = 2\pi/k_c$ (two cells), for Newtonian and Carreau fluids at a reduced Reynolds number $\epsilon = 0.1$. Positive and negative values of ψ correspond to anticlockwise and clockwise rotation. The vortices lose the symmetry along the horizontal axis through the cell center. The eye of vortices is shifted towards upper and lower cell boundaries, i.e. $z/\lambda_z = 0$ and 1. This effect is weak for a Newtonian fluid (figure 18(a) and becomes more pronounced with decreasing the shear-thinning index n_c. This axial shift of the vortex eye is coupled with the radial shift towards the inner cylinder due to the viscosity stratification discussed in § II.3. The displacement of the vortex center in the direction of higher shear-stress and lower viscosity leads to an increasing concentration of vorticity near the inner wall at $z/\lambda_z = 0$ and 1 as it is shown in figure 19 where isolines of contours of Ω are displayed for different rheological parameters. In contrast with the build-up of vorticity near the inner cylinder and at the corners $z = 0$ and $z = \lambda_z$, the region between the two cells, around $z/\lambda_z = 0.5$, which is practically void of vorticity increases in area with increasing shear-thinning effects.

This build-up of the vorticity with increasing shear-thinning effects and the change in the vortices can be related to the evolution of the radial flow from the inner to the outer cylinder (outflow) at $z/\lambda_z = 0$ and $z/\lambda_z = 1$ and from the outer to the inner one (inflow), around $z/\lambda_z = 0.5$. Figure 20 shows the radial velocity component at the vortex eye center, versus z for Newtonian and Carreau fluids. It can be observed that the radial outflow is stronger than the radial inflow.

The ratio r_u between the intensity ($\max|u|$) of the radial outflow and that the radial inflow, increases with increasing shear-thinning effects. At $\epsilon = 0.1$, r_u increases from 1.6 for a New-

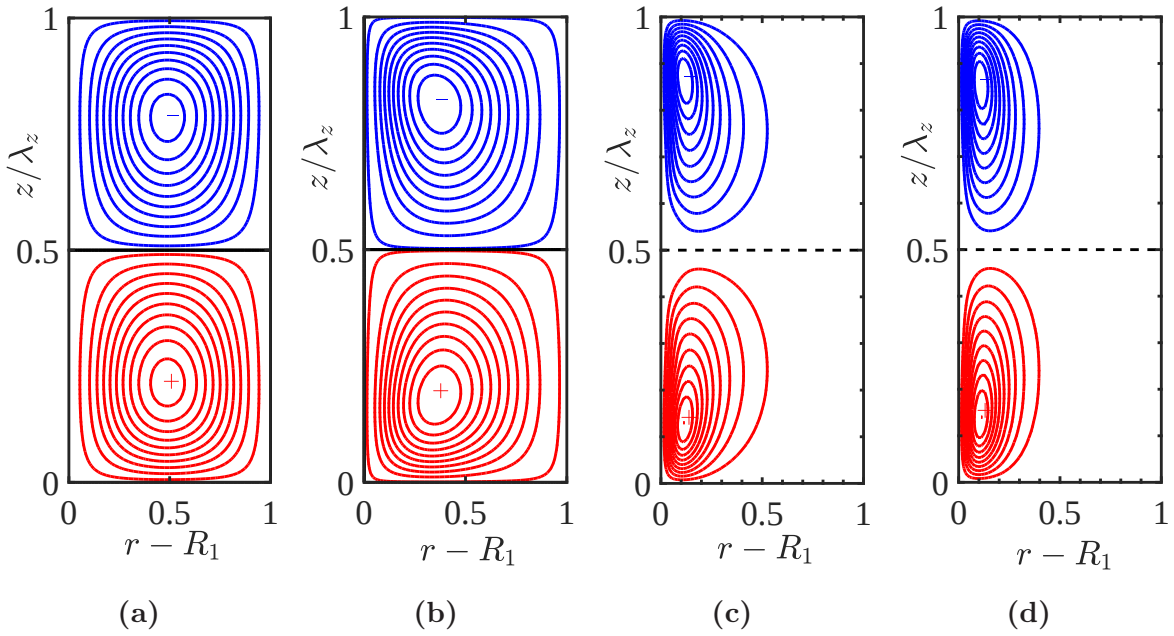

FIG. 18: (Color online) Contours of streamfunction at $\epsilon = 0.1$ for **(a)** Newtonian fluid, with ($\psi_{max} = 2.2\,10^{-2}$); **(b)** Carreau fluid with $n_c = 0.5$, $\lambda = 1$ ($\psi_{max} = 1.05510^{-2}$); **(c)** Carreau fluid with $n_c = 0.2$, $\lambda = 1$, ($\psi_{max} = 2.082\,10^{-3}$) ; **(d)** Carreau fluid with $n_c = 0.2$, $\lambda = 10$, ($\psi_{max} = 2.1\,10^{-3}$). The increment between lines is $\Delta\,\psi = \psi_{max}/10$.

tonian fluid to 4.5 for a Carreau fluid with $n_c = 0.2$ and $\lambda = 10$. The width of the radial outflow zone decreases with decreasing n_c and the region of inflow increases accordingly. For instance, at $\epsilon = 0.1$ and for a Carreau fluid with $n_c = 0.2$ and $\lambda = 10$, the ratio between the axial extent of radial outflow and that of inflow is practically 3, whereas for a Newtonian fluid, the ratio is slightly larger than 1. With increasing Reynolds number $\mathcal{R}$, the radial outflow becomes stronger, increasingly jet-like, and the ratio r_u between $\max|u|$ in outflow and inflow increases. At $\epsilon = 0.3$, $r_u \approx 6.5$ for a Carreau fluid with $n_c = 0.2$, $\lambda = 10$, whereas for a Newtonian fluid, $r_u \approx 2.1$.

Fluctuations in the radial inflow, observed with decreasing n_c, might be related to the influence of harmonics discussed in the Section V.7.

The change of the flow with increasing shear-thinning effects is also shown from consideration of the azimuthal velocity distribution. Contours of v are displayed in figure 22 for Newtonian and Carreau fluids at $\epsilon = 0.1$. Positive azimuthal streaks evolve in the outflow region, $z/\lambda_z = 0$ and 1, where high azimuthal momentum fluid is carried outward from near the inner cylinder. Similarly, negative azimuthal streak evolves in the inflow region,

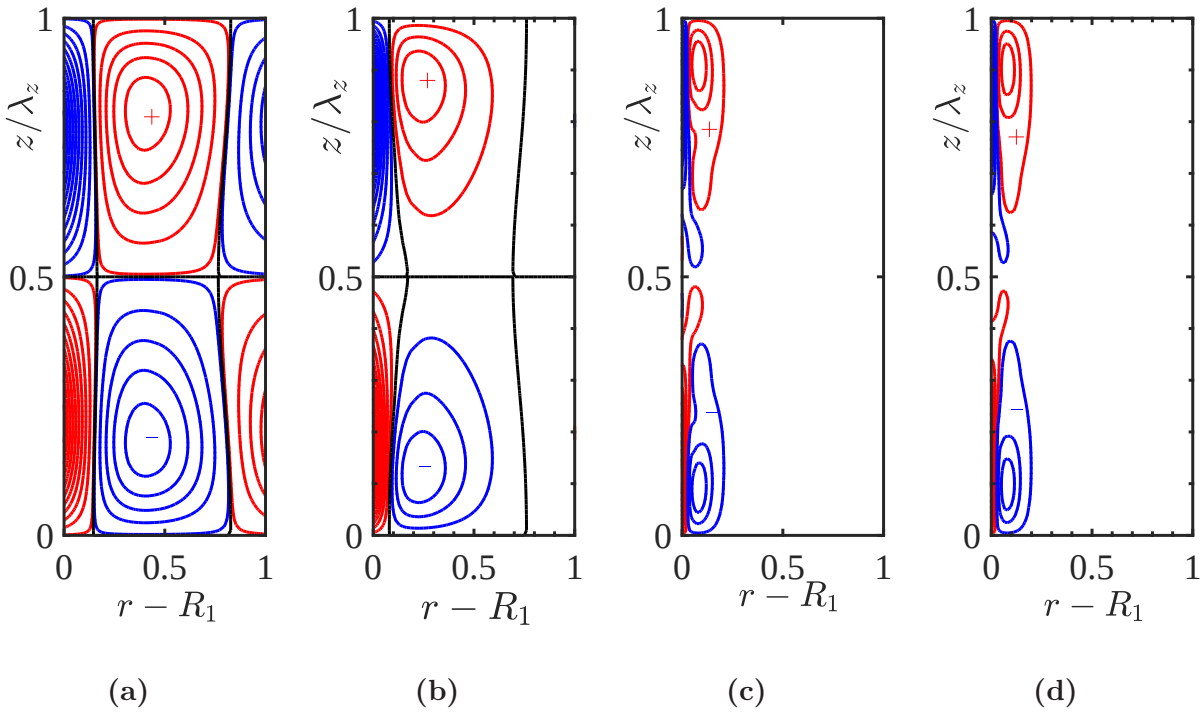

FIG. 19: (Color online) Contours of vorticity for **(a)** Newtonian fluid, $n_c = 1$, with $\Omega_{max} = 1.121$; **(b)** Carreau fluid with $n_c = 0.5$, $\lambda = 1$, $\Omega_{max} = 1.625$; **(c)** Carreau fluid with $n_c = 0.2$, $\lambda = 1$, $\Omega_{max} = 3.965$; **(d)** Carreau fluid with $n_c = 0.2$, $\lambda = 10$, $\Omega_{max} = 4.199$. The increment between lines is $\Delta\,\Omega = \Omega_{max}/10$.

$z/\lambda_z = 0.5$, where low azimuthal momentum fluid is carried inward from near the outer cylinder. With increasing shear-thinning effects, contours lines of v are more concentrated in the vicinity of the inner cylinder, and the positive azimuthal streaks of narrow width are separated by a negative streak of a large extent. The evolution of the positive and negative azimuthal streaks with increasing Reynolds number is illustrated by plotting in figure 23 the axial profile of v at a fixed radial position (center of patterns) and different values of ϵ. The positive azimuthal streak increases strongly with ϵ and shear-thinning effects, whereas v varies relatively little in the inflow region. This asymmetry between the inflow and the outflow can be described in terms of local Reynolds number defined with the local azimuthal velocity and the local viscosity.

The influence of shear thinning effects on the flow structure is also illustrated by contours of the axial component of the velocity w, represented in the figure 24. With increasing the shear-thinning behavior, the maximum of w is shifted radially towards the inner cylinder and axially towards the outflow boundaries $z/\lambda_z = 0\,\text{and}\,1$. Hence, in a very thin region

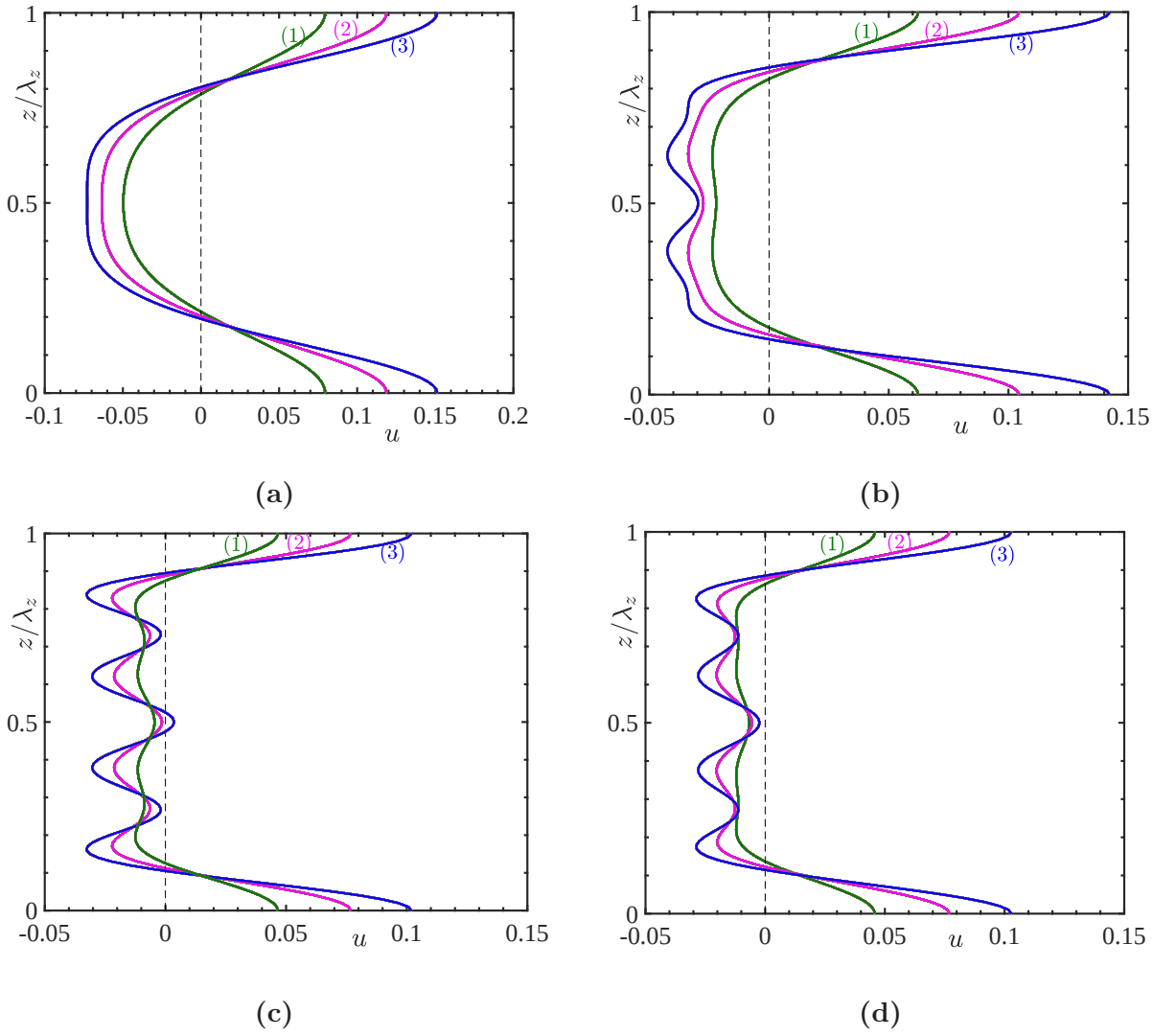

FIG. 20: (Color online) Radial component of velocity versus z at a fixed radial position corresponding to the vortex eye center. **(a)** Newtonian fluid; **(b)** Carreau fluid with $n_c = 0.5$, $\lambda = 1$; **(c)** Carreau fluid with $n_c = 0.2$, $\lambda = 1$; **(d)** Carreau fluid with $n_c = 0.2$, $\lambda = 10$. (1) $\mathcal{R} = 1.1\,\mathcal{R}_c$, (2) $\mathcal{R} = 1.2\,\mathcal{R}_c$, (3) $\mathcal{R} = 1.3\,\mathcal{R}_c$

across the outflow boundary, w changes from positive extremum to negative extremum and vice versa.

The change in the flow structure with $\mathcal{R}$ and shear-thinning effects modifies the second invariant Γ of strain-rate tensor $\dot{\gamma}$ and therefore the viscosity. Analysis of the different components $\dot{\gamma}_{ij}$ show that Γ is dominated by the term $(\dot{\gamma}_{r\theta}(\boldsymbol{U_b} + \boldsymbol{u}))^2 \approx (\dot{\gamma}^b{}_{r\theta})^2 + 2\dot{\gamma}^b_{r\theta}\dot{\gamma}_{r\theta}$. In the outflow region, according to the contours of the azimuthal velocity (22), $\dot{\gamma_{r\theta}}(u)$ is positive and maximum at the inner cylinder ($\Gamma < \Gamma_b$), then decreases, vanishes ($\Gamma = \Gamma_b$) around the

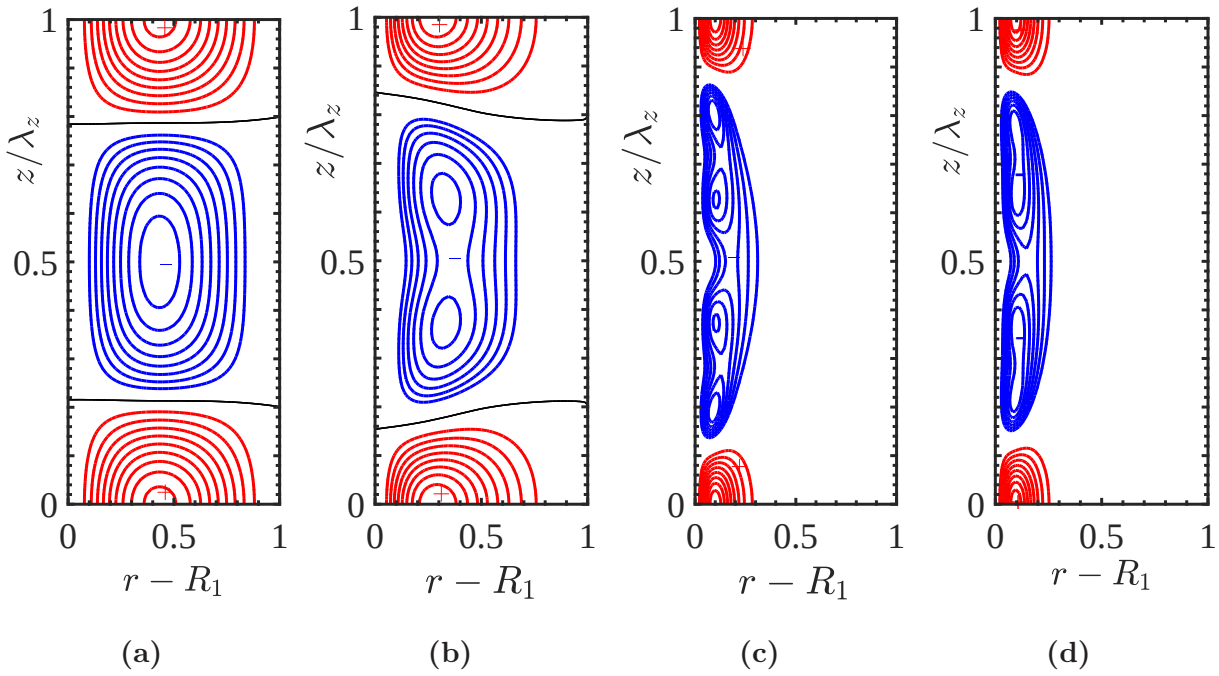

FIG. 21: (Color online) Contours of radial velocity component at $\epsilon = 0.1$ for **(a)** Newtonian fluid, $u_{max} = 0.077$, $u_{min} = -0.049$; **(b)** Carreau fluid with $n_c = 0.5$, $\lambda = 1$, $u_{max} = 0.057$, $u_{min} = -0.021$; **(c)** Carreau fluid with $n_c = 0.2$, $\lambda = 1$, $u_{max} = 0.0466$, $u_{min} \approx -0.012$; **(d)** Carreau fluid with $n_c = 0.2$, $\lambda = 10$, $u_{max} = 0.046$, $u_{min} = -0.012$. The increment between lines is $\Delta u = u_{max}/10$ for positive values and $\Delta u = u_{min}/10$ for negative values.

center of the pattern, and becomes negative ($\Gamma > \Gamma_b$). Similar description can be done for the inflow region, but with opposite signs. This variation of Γ explains the shape of the viscosity contours (Figure 25). For sufficiently strong shear-thinning effects, the vortices are confined near the inner cylinder with a quite large fluid layer adjacent to the outer cylinder where the perturbation is practically inexistent. In this case, the viscosity contours remain straight lines near the outer cylinder as it is shown by figure 25 (b) where the viscosity contours are represented at $\epsilon = 0.1$ for a Carreau fluid with $n_c = 0.2$ and $\lambda = 10$.

V.7. Harmonics

Nonlinearities of inertial and viscous terms generate spatial harmonics (in the axial direction) of the fundamental mode. From equations (58), (64), (65) and (69), the flow variables

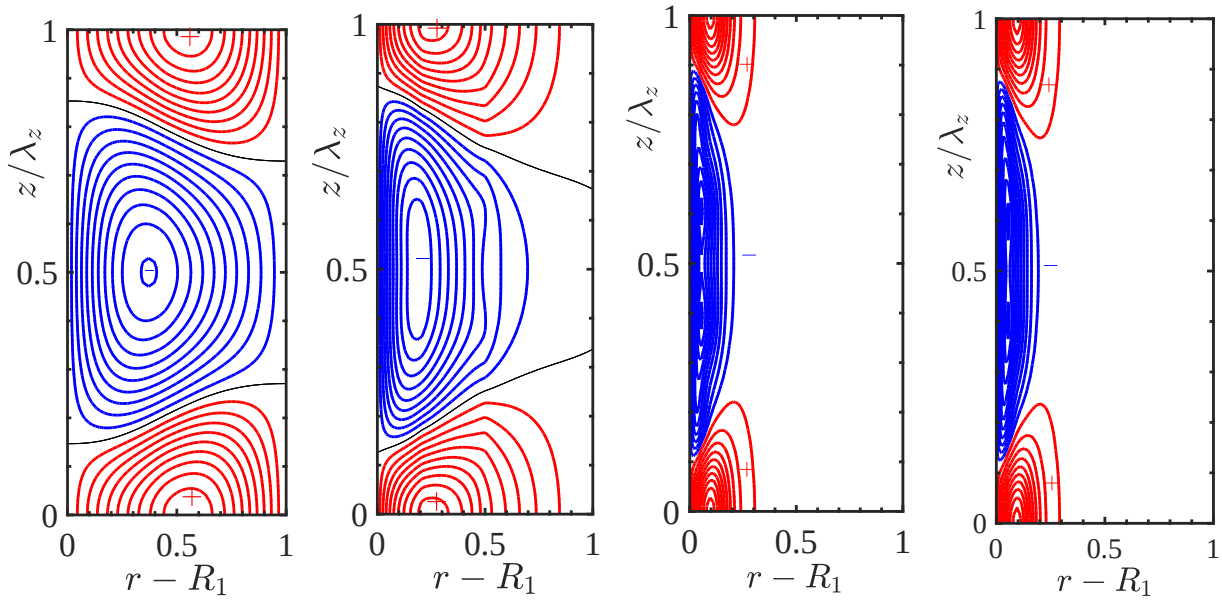

FIG. 22: (Color online) Contours of azimuthal velocity v at $\epsilon = 0.1$ for **(a)** Newtonian fluid, $v_{max} \approx 0.1$, $v_{min} \approx -0.12$; **(b)** Carreau fluid with $n_c = 0.5$, $\lambda = 1$, $v_{max} = 0.11$, $v_{min} \approx -0.093$; **(c)** Carreau fluid with $n_c = 0.2$, $\lambda = 1$, $v_{max} \approx 0.225$, $v_{min} \approx -0.12$; **(d)** Carreau fluid with $n_c = 0.2$, $\lambda = 10$. The increment between lines is $\Delta v = v_{max}/10$ for positive values and $\Delta v = v_{min}/10$ for negative values .

(u, v, w) can be written as sum of Fourier components. For instance for v:

$$v(r, z) = v_0(r) + \sum_{n=1}^{\infty} v_n \cos nk_c z \tag{95}$$

with

$$v_0 = \sum_{m=0}^{\infty} A^{2m} V_{0,2m} \quad \text{and} \quad v_n = 2 \sum_{m=0}^{\infty} A^{2m+n} V_{n,2m+n}. \tag{96}$$

The amplitude A is the stationary solution of the amplitude equation (68). The form of the u-component is similar to v except that v_0 is omitted. The w-component is like u except that the z-dependency is in $\sin nk_c z$. In order to describe the growth of harmonics with Reynolds number, the Fourier amplitude v_n in (95) are averaged over the gap width, as in [48] and [6],

$$\overline{v_n} = \frac{1}{R_2 - R_1} \int_{R_1}^{R_2} v_n(r) r \mathrm{d}r. \tag{97}$$

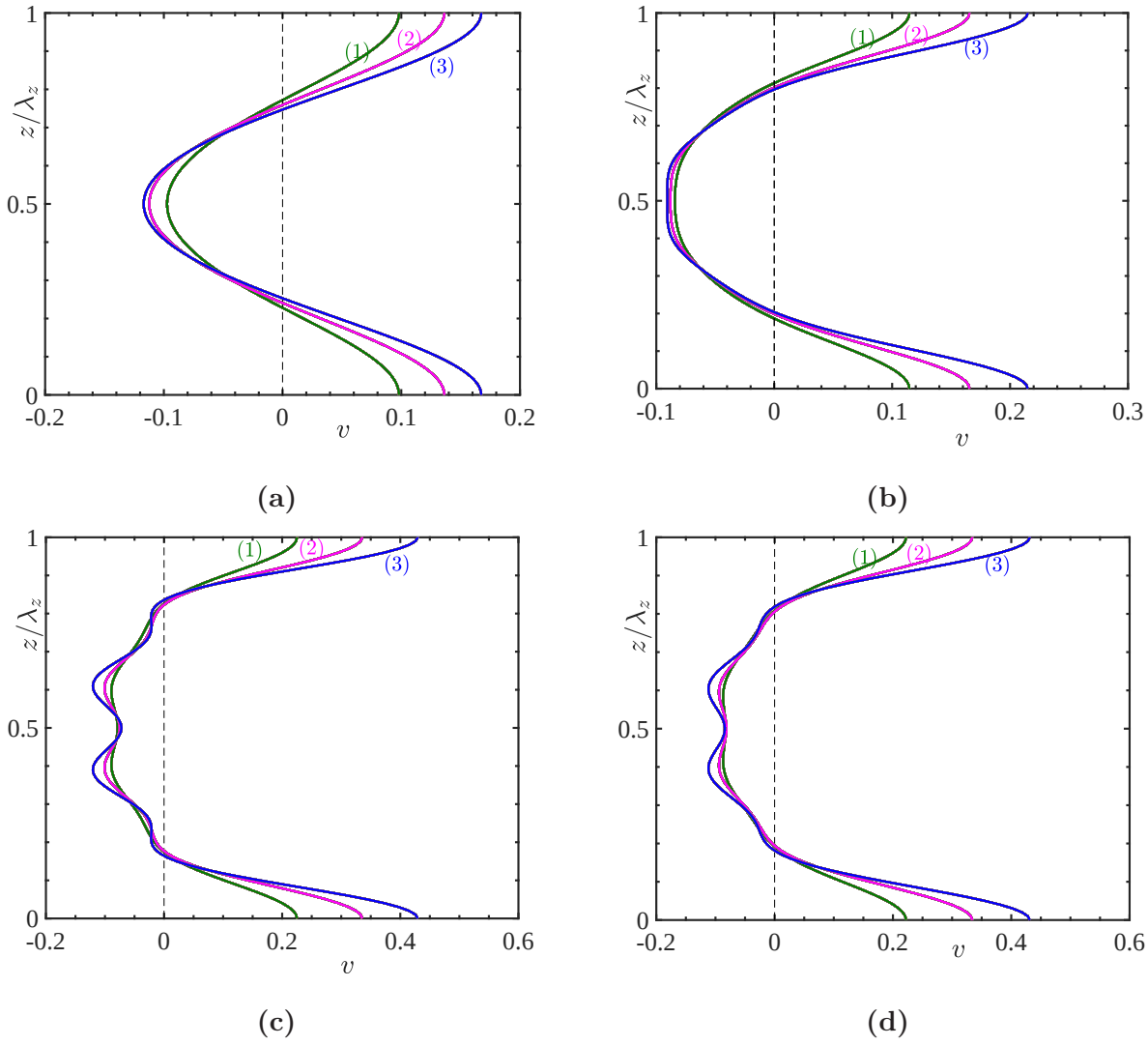

FIG. 23: (Color online) Azimuthal component of velocity versus z at fixed radial position (center of pattern) and different Reynolds number. **(a)** n = 1 Newtonian fluid, **(b)** Carreau fluid with $n_c = 0.5$, $\lambda = 1$, **(c)** Carreau fluid with $n_c = 0.2$, $\lambda = 1$, **(d)** Carreau fluid with $n_c = 0.2$, $\lambda = 10$. (1) $\mathcal{R} = 1.1\,\mathcal{R}_c$, (2)$\mathcal{R} = 1.2\,\mathcal{R}_c$, (3) $\mathcal{R} = 1.3\,\mathcal{R}_c$

We recall that v_0 corresponds to the modification of the base flow, v_1 to the distorted fundamental mode, v_2 to the second harmonic, etc ... In Figure 26, we have represented, the growth of the averaged Fourier amplitudes as the Reynolds number is increased, for Newtonian and shear-thinning fluids. The initial amplification of the fundamental mode $n = 1$ is stronger for a Newtonian fluid than for a shear-thinning fluid. At $\epsilon = 0.3$, $\overline{u_1}$(Newtonian fluid) $\approx 10 \times \overline{u_1}$(shear-thinning fluid). The zeroth-mode becomes more significant as the Reynolds number is raised. For example, at $\epsilon = 0.3$, $\overline{v_0} = 0.77 \times \overline{v_1}$ for a

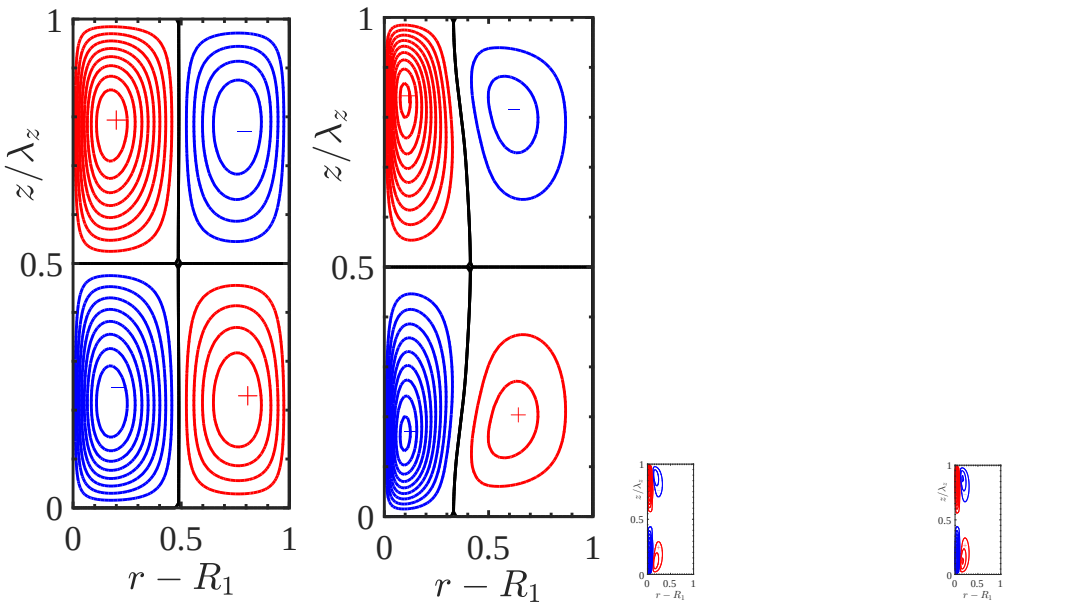

FIG. 24: (Color online) Contour of axial velocity component w at $\epsilon = 0.1$ for **(a)** Newtonian fluid, $w_{max} = 0.082$; **(b)** Carreau fluid with $n_c = 0.5$, $\lambda = 1$, $w_{max} = 0.063$; **(c)** Carreau fluid with $n_c = 0.2$, $\lambda = 1$, $w_{max} = 0.05$, **(d)** Carreau fluid with $n_c = 0.2$, $\lambda = 10$, $w_{max} = 0.048$. The increment between lines is $\Delta w = w_{max}/10$ for positives values and $\Delta w = -w_{max}/10$ for negative values.

Newtonian fluid and $\overline{v_0} = 0.84 \times \overline{v_1}$ for the shear-thinning fluid. Higher harmonics, $n = 2$, 3, 4 grow faster with Reynolds number for shear-thinning fluids than for a Newtonian fluid. Note also in figure 26 (d) that for sufficiently strong shear-thinning behavior, the harmonic numbered (4) may overtake the harmonic numbered (3).

All in all, nonlinearities of the viscous terms combined with that of the inertial terms lead to a stronger amplification of higher harmonics.

VI. CONCLUSION

Taylor-vortex flow (TVF) regime in shear-thinning fluids is considered in the present work. We focused mainly on the wide gap configuration. The fluid is assumed purely viscous. Compared to the Newtonian case, an additional nonlinearity appears in the momentum equations, via the rheological law. This additional nonlinearity is more complex than the quadratic nonlinear inertial terms. A weakly nonlinear analysis is used as a first

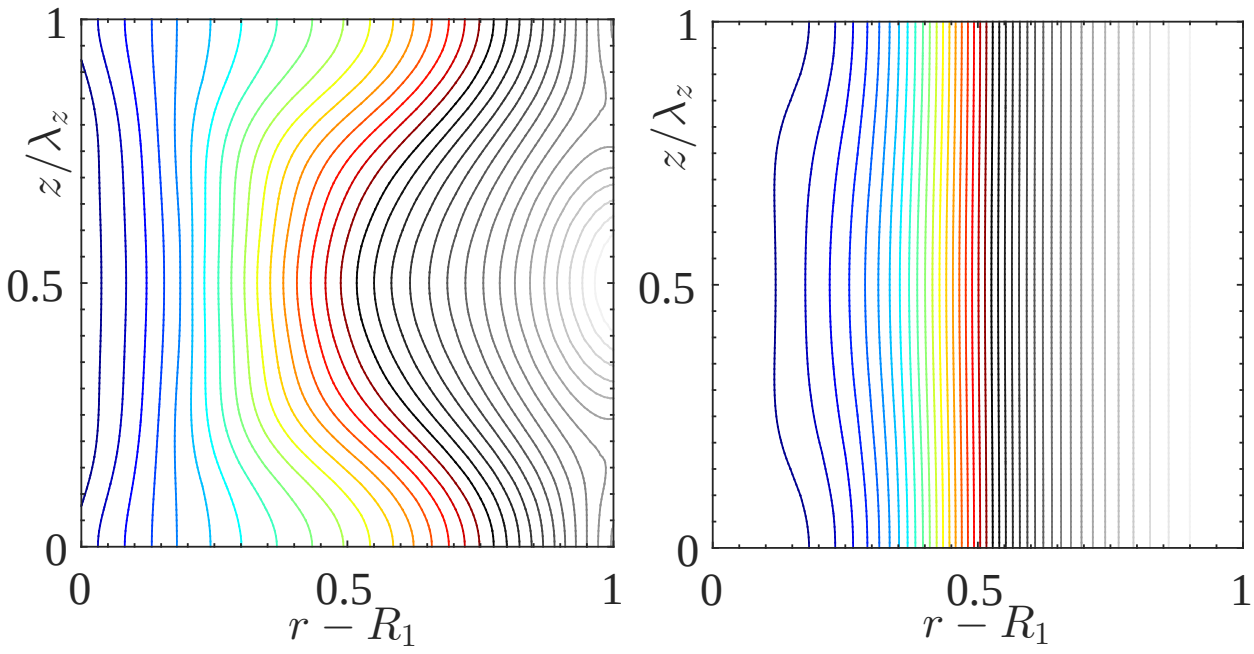

FIG. 25: (Color online) **(a)**Viscosity contours at $\epsilon = 0.1$ for: Carreau fluid with $n_c = 0.5$, $\lambda = 1$, $\mu_{max} = 0.63$, $\mu_{min} = 0.094$, the increment between lines is $\Delta\,\mu = 0.015$. **(b)** Carreau fluid with $n_c = 0.2$, $\lambda = 10$, $\mu_{min} = 0.0046$, $\mu_{max} = 0.86$, the increment between lines is $\Delta\,\mu = 0.02$.

approach to take into account nonlinear effects. The amplitude expansion Landau-Stuart method is adopted. The Carreau model is used as a typical rheological model.

As a first step, the critical Reynolds number, $\mathcal{R}_c$, for the onset of Taylor vortices was determined for a large range of rheological parameters. It is shown that, $\mathcal{R}_c$ defined with the zero shear viscosity decreases with increasing shear-thinning effects. This is the consequence of the increase of the shear-rate and decrease of the viscosity near the inner wall. Furthermore, the characteristic time for the growth of the vortices increases significantly with increasing shear-thinning effects. Computation of the first Landau coefficient g_1, indicates that it is dominated by the feedback of the base flow correction onto the fundamental mode, when the Newtonian fluid is considered. For a shear-thinning fluids, the feedback of the first harmonic becomes more and more significant as the shear-thinning index decreases. The kinetic energy ξ of the fundamental mode was determined. It is shown that ξ decreases with increasing shear-thinning effects and more than 90 % of ξ is concentrated on the azimuthal

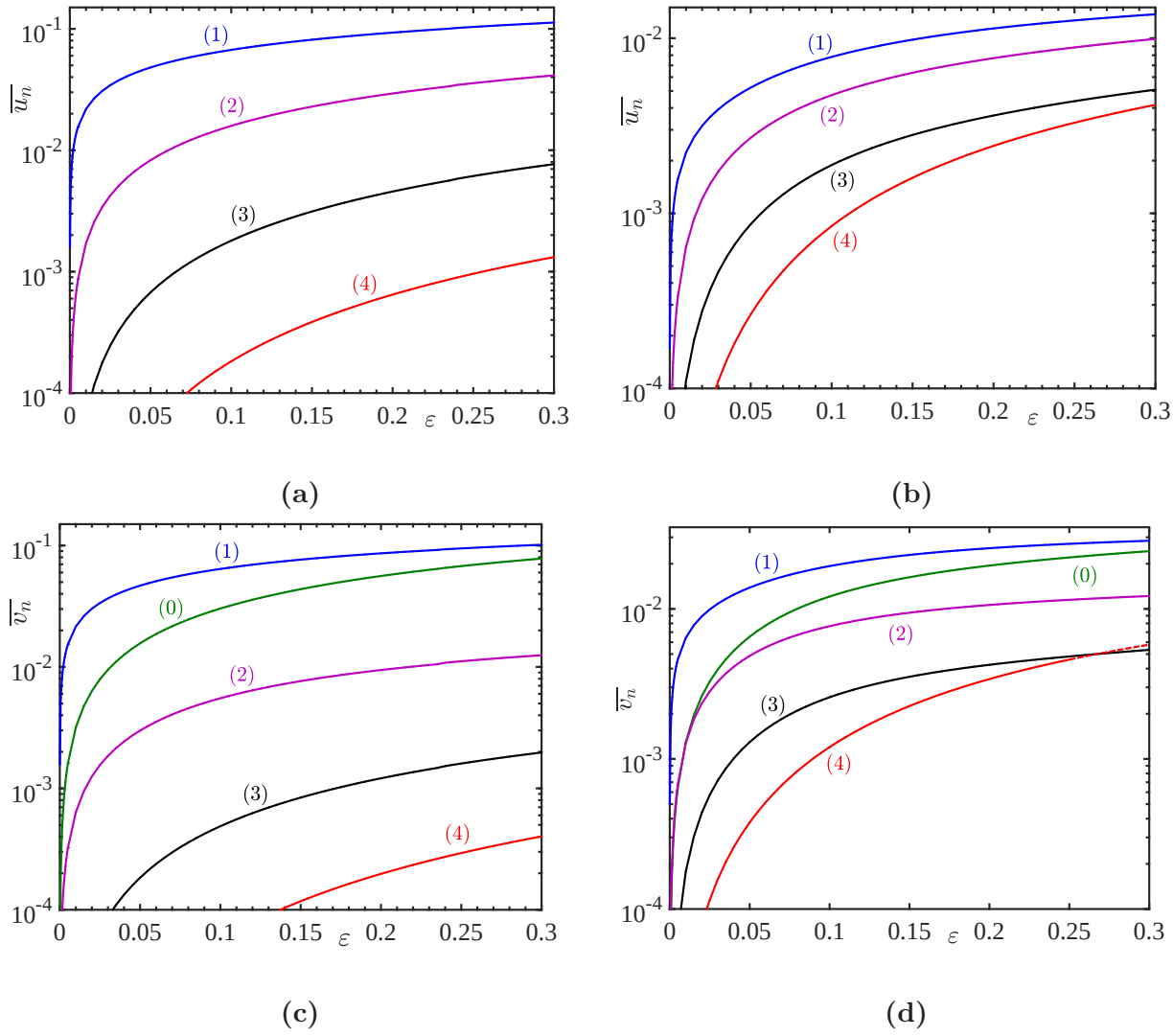

FIG. 26: (Color online) Evolution of the harmonics (averaged over a width gap) as a function of the reduced Reynolds number for a Newtonian fluid, frame **(a)** and **(c)** and a Carreau fluid, frame **(b)** and **(d)**, with $n_c = 0.2$, $\lambda = 10$.

component.

Detailed analysis of the flow structure in the TVF regime at moderate distance from the onset was obtained by considering amplitude equation at seventh-order. It is shown that with increasing shear-thinning effects, Taylor vortices are squeezed against the inner cylinder and the center of the patterns are axially shifted towards the outflow boundaries ($z = 0$, $z/\lambda_z = 1$). Associated with this shift of the patterns is the increasing concentration of vorticity at these positions. Furthermore, the outflow becomes more stronger than the inflow and the area of the inflow increases accordingly. Positive azimuthal streaks induced

by the radial outflow is more and more significant. Whereas, the negative azimuthal streak is weak and occupies a large region. The change in the flow structure modifies the viscosity field. The numerical results show that this modification is mainly related to the variation of the shear-rate $\dot{\gamma}_{r\theta}(\boldsymbol{U_b} + \boldsymbol{u})$. The pseudo-Nusselt number Nu_* is another feature of the flow structure. It is found that Nu_* decreases with increasing shear-thinning effects. Besides this, analysis of the Fourier coefficients shows that even at moderate distance from the onset, higher harmonics become more relevant comparatively to the Newtonian case.

Additional computations were performed for a narrow gap configuration. In this case, the azimuthal velocity profiles of the base flow get close to the linear profile, the viscosity stratification is weak and the range of $\mathcal{R}$ where the TVF regime is stable is quite limited. According to Coles [49] and Jones [5], for $\eta \geq 0.9$, transition to wavy vortex flow is observed at $\mathcal{R} \approx 1.2\,\mathcal{R}_c$ ($\epsilon = 0.2$). Some results are reported in Appendix D for radius ratio $\eta = 0.9$. For strong shear-thinning effects, the marginal stability curve flattens and the coherence length of the perturbation decreases significantly. In this case, modes of different wavenumbers (delimited by the Eckhaus boundary) exist close to the onset of the primary bifurcation. These modes may interact with each other leading to a secondary bifurcation with a more complex dynamic. The interaction of modes of different wavenumber limits the range of validity of the weakly nonlinear analysis. Nevertheless, we think that the modifications of the flow structure described in this study plays a fundamental role in triggering an eventual secondary bifurcation. To understand the interaction between different modes, a fully nonlinear method based on the numerical continuation can be used [50]. This approach could be useful to clarify the influence of shear-thinning on the coupling between the fundamental mode and the second harmonic observed experimentally by Crumeyrolle et al. [51] for semi-dilute aqueous solutions of high molecular weight polyethylenoxide.

Appendix A: Validation

Radius ratio η	Chandrasekhar [38] $(\mathcal{R}_c)$	Our results $(\mathcal{R}_c)$
$\eta = 0.975$	260.9476	260.9496
$\eta = 0.950$	184.98	184.99
$\eta = 0.925$	151.48	151.4772
$\eta = 0.900$	131.6131	131.6145
$\eta = 0.875$	118.157	118.1571
$\eta = 0.850$	108.3119	108.3131
$\eta = 0.750$	85.7764	85.7765
$\eta = 0.650$	74.9622	74.9623
$\eta = 0.500$	68.1862	68.1863

TABLE I: Newtonian fluid. Critical Reynolds number at different radius ratios. Comparison with Chandrasekhar's results [38]

.

Rheological parameters	Alibenyahia et al. [16] $(\mathcal{R}_c)/\mu_w$	Our results $(\mathcal{R}_c)/\mu_w$
$n = 0.7$, $\lambda = 20$	260.9476	260.9496
$n = 0.5$, $\lambda = 20$	184.98	184.99
$n = 0.3$, $\lambda = 20$	151.48	151.4772

TABLE II: Carreau fluid. Critical Reynolds number defined with the inner wall shear viscosity. Comparison with Alibenyahia et al. [16]

.

Appendix B: Contribution of nonlinear inertial and nonlinear viscous terms

The feedback of the mean flow correction and that of the first harmonic on the fundamental mode through the nonlinear inertial and nonlinear viscous terms are given in table IV for $\lambda = 10$ and different values of the shear-thinning index n_c.

$\mathcal{R}$	Nu_* Our results	Nu^* Donnelly & Simon [45]
69.1	1.012422	1.016190
70.2	1.027175	1.024306
73.0	1.063204	1.053082
75.3	1.090811	1.076942
78.8	1.129259	1.111199
85.1	1.188594	1.167744
94.8	1.260240	1.246044
107.0	1.326927	1.279206
121.0	1.383261	1.394628

TABLE III: Newtonian fluid. Variation of the Pseudo-Nusselt number Nu_* versus Reynolds number at $\eta = 0.5$. Comparison between our results and those obtained experimentally by Donnelly & Simon [45]

n_c	g_1	g_{10}^I	g_{10}^V	g_{12}^I	g_{12}^V	g_{1-11}^V
0.2	-38.235	-29.561	6.721	-28.098	25.534	-12.831
0.3	-53.698	-33.737	5.724	-42.354	26.268	-9.598
0.4	-76.801	-45.024	3.527	-52.555	24.690	-7.438
0.5	-108.301	-65.101	9.766	-60.968	22.549	-5.758
0.6	-151.688	-95.215	-1.276	-71.688	20.446	-3.956
0.7	-214.583	-140.846	-3.006	-86.899	18.018	-1.849
0.8	-315.127	-215.481	-4.105	-110.776	14.775	4.592
0.9	-496.243	-351.458	-3.970	-152.723	9.693	2.216
1.0	-867.033	-632.705	0.000	-234.329	0.000	0.000

TABLE IV: Cubic Landau constant and contributions of nonlinear inertial and nonlinear viscous terms at the critical conditions

Appendix C: Landau constants

The Landau coefficients g_1, g_2, g_3 are given in table V for $\lambda = 10$ and different values of the shear-thinning index.

n_c	g_1	g_2	g_3
0.2	-38.217	-11496.709	-2411946.180
0.3	-53.698	-16939.108	-5604408.660
0.4	-76.647	-21517.202	-8480701.020
0.5	-108.271	-25742.819	-10761822.517
0.6	-151.684	-31643.773	-13182598.598
0.7	-214.583	-33736.107	-12116764.641
0.8	-315.127	-38383.606	-11625135.458
0.9	-496.243	-48609.312	-12000787.340
1.0	-867.033	-62111.466	-12310212.318

TABLE V: Landau constants at the critical conditions for different values of the shear-thinning index

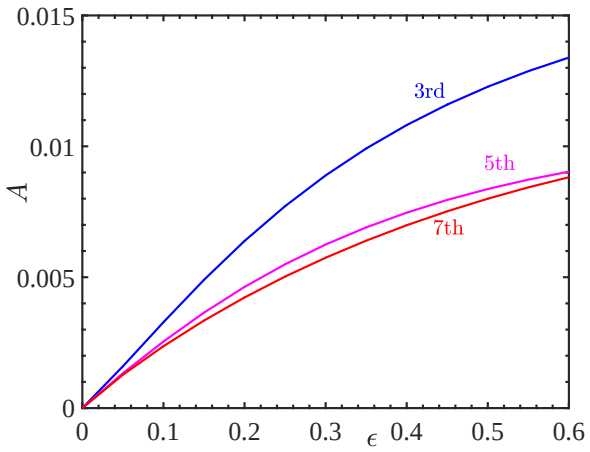

FIG. 27: (Color online) Evolution of the amplitude A versus $\epsilon = (\mathcal{R} - \mathcal{R}_c)/\mathcal{R}_c$ for a shear-thinning fluid with $n_c = 0.5$, $\lambda = 10$, at cubic, fifth and seventh-order in the amplitude expansion.

Appendix D: Flow structure and viscosity field for $\eta = 0.9$

In the figure 28 we have represented contours of the stream function, the vorticity and the viscosity distribution at $\epsilon = 0.1$, for a Carreau fluid with $n_c = 0.2$ and $\lambda = 10$.

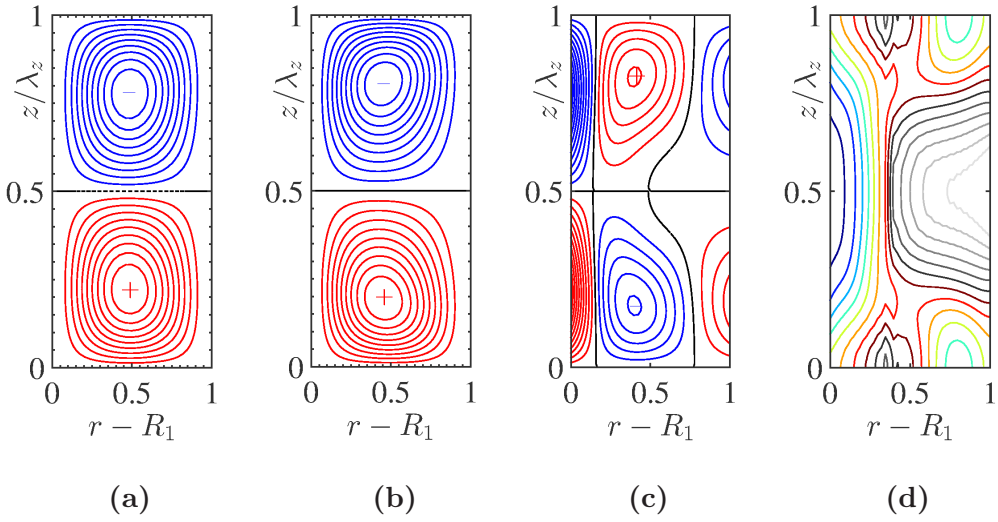

FIG. 28: (Color online) Narrow gap, $\eta = 0.9$. Flow field structure for a Newtonian fluid and a Carreau fluid with $n_c = 0.2$, $\lambda = 10$. **(a)** Contours of the stream function for a Newtonian fluid, $\psi_{max} = 0.12$, $\Delta\psi = \psi_{max}/10$. **(b)** Contours of the stream function for the Carreau fluid,$\psi_{max} = 0.072$, $\Delta\psi = \psi_{max}/10$. **(c)** Contours of vorticity for a Carreau fluid, $\Omega_{max} = 0.35$, $\Delta\Omega = \Omega_{max}/10$. **(d)**, Contours of the viscosity for the Carreau fluid, $\mu_{max} = 0.0843$, $\mu_{min} = 0.02$, $\Delta\mu = 0.004$.

---

[1] E. L. Koschmieder. Bénard cells and Taylor vortices. *Cambridge Monographs on Mechanics and Applied Mathematics. Cambridge University Press.*, 844:37–51, 1993.

[2] R. Tagg. The Couette-Taylor problem. *Nonlinear Sci. Today*, 4:1–25, 1994.

[3] P. G. Drazin and W. H. Reid. Hydrodynamic stability. *Cambridge Mathematical Library. Cambridge University Press.*, 1981.

[4] G. I. Taylor. Stability of a viscous liquid contained between two rotating cylinders. *Trans. R. Soc. Lond. A*, 223:289–343, 1923.

[5] C. A. Jones. The transition to wavy Taylor vortices. *J. Fluid Mech.*, 157:135–162, 1985.

[6] H.A. Snyder and R.B. Lambert. Harmonic generation in Taylor vortices between rotating cylinders. *J. Fluid Mech.*, 26(3):545–562, 1966.

[7] O. Meincke and C. Egbers. Routes into chaos in small and wide gap Taylor-Couette flow. *Physics and Chemistry of the Earth, Part B: Hydrology, Oceans and Atmosphere*, 24(5):467–471, 1999.

[8] C. D. Andereck, S. S. Liu, and H. L. Swinney. Flow regimes in a circular Couette system with independently rotating cylinders. *J. Fluid Mech.*, 164:155–183, 1986.

[9] H. Giesekus. Zur stabilität von strömungen viskoelastischer flüssigkeiten. *Rheol. Acta*, 5(3):239–252, 1966.

[10] S. J. Muller, R.G. Larson, and E.S.G. Shaqfeh. A purely elastic transition in Taylor-Couette flow. *Rheol. Acta*, 28(6):499–503, 1989.

[11] R.G. Larson, E.S.G. Shaqfeh, and S.J. Muller. A purely elastic instability in Taylor-Couette flow. *J. Fluid Mech.*, 218:573–600, 1990.

[12] E.S.G. Shaqfeh, S.J. Muller, and R.G. Larson. The effects of gap width and dilute solution properties on the viscoelastic Taylor-Couette instability. *J. Fluid Mech.*, 235:285–317, 1992.

[13] A. Groisman and V. Steinberg. Mechanism of elastic instability in Couette flow of polymer solutions. *Phys. Fluids*, 10:2451–2463, 1998.

[14] A. Lindner, D. Bonn, and J. Meunier. Viscous fingering in a shear-thinning fluid. *Phys. Fluids*, 12(2):256–261, 2000.

[15] Y. Agbessi, B. Alibenyahia, C. Nouar, and L. Choplin. Linear stability of Taylor-Couette flow of shear-thinning fluids: modal and non-modal approaches. *J. Fluid Mech.*, 775:354–389, 2015.

[16] B. Alibenyahia, C. Lemaître, C. Nouar, and N. Ait-Messaoudene. Revisiting the stability of circular Couette flow of shear-thinning fluids. *J. Non-Newtonian Fluid. Mech.*, 183:37–51, 2012.

[17] Z. Li and R.E. Khayat. A non-linear dynamical system approach to finite amplitude Taylor-Vortex flow of shear-thinning fluids. *Int. J. Numer. Methods Fluids*, 45(3):321–340, 2004.

[18] N. Ashrafi and R.E. Khayat. Shear-thinning-induced chaos in Taylor-Couette flow. *Phys. Rev. E*, 61(2):1455, 2000.

[19] N. Ashrafi. Stability analysis of shear-thinning flow between rotating cylinders. *Appl. Math. Model*, 35(9):4407–4423, 2011.

[20] N. Ashrafi. Effect of nonlinearity on the Taylor-Couette flow in the narrow-gap. *J. Mech. Sci. Technol.*, 25(9):2247, 2011.

[21] H. Masuda, T. Horie, R. Hubacz, M. Ohta, and N. Ohmura. Prediction of onset of Taylor-Couette instability for shear-thinning fluids. *Rheol. Acta*, 56(2):73–84, 2017.

[22] M. P. Escudier, I. W. Gouldson, and D. M. Jones. Taylor vortices in Newtonian and shear-thinning liquids. *Proc. Roy. Soc. Lond. A.*, 449:155–176, 1995.

[23] V. Sinevic, R. Kuboi, and A.W. Nienow. Power numbers, Taylor numbers and Taylor vortices in viscous Newtonian and non-Newtonian fluids. *Chem. Eng. Sci.*, 41(11):2915–2923, 1986.

[24] N. Cagney and S. Balabani. Taylor-Couette flow of shear-thinning fluids. *Phys. Fluids*, 31(5):053102, 2019.

[25] J. Watson. On the non-linear mechanics of wave disturbances in stable and unstable parallel flows. part 1. the development of a solution for plane Poiseuille flow and for plane Couette flow. *J. Fluid Mech.*, 9:371–389, 1960.

[26] J. T. Stuart. On the non-linear mechanics of wave disturbances in stable and unstable parallel flows. part 1. the basic behaviour in plane Poiseuille flow. *J. Fluid Mech.*, 9:353–370, 1960.

[27] T. Herbert. On perturbation methods in nonlinear stability theory. *J. Fluid Mech.*, 126:167–186, 1983.

[28] P.K. Sen and D. Venkateswarlu. On the stability of plane Poiseuille flow to finite-amplitude disturbances, considering the higher-order Landau coefficients. *J. Fluid Mech.*, 133:179–206, 1983.

[29] K. Fujimura. The equivalence between two perturbation methods in weakly nonlinear stability theory for parallel shear flows. *Proc. R. Soc. Lond. A*, 424(1867):373–392, 1989.

[30] P. Chossat and G. Iooss. *The Couette-Taylor Problem*, volume 102. Springer Science & Business Media, 2012.

[31] P.J. Carreau. Rheological equations from molecular network theories. *Transactions of the Society of Rheology*, 16(1):99–127, 1972.

[32] R. B. Bird, R. Amstrong, and O. Hassager. *Dynamics of polymeric liquids*. Wiley-Interscience, New York, 1987.

[33] R. Tanner. Engineering rheology. Oxford University Press, New York, 2000.

[34] M. Darbouli, C. Métivier, S. Leclerc, C. Nouar, M. Bouteraa, and S. Didier. Natural convection in shear-thinning fluids: Experimental investigations by MRI. *Int. J. Heat Mass Transfer*, 95:742–754, 2016.

[35] A.S. Haase, A.J. Wood, L.M.J. Sprakel, and R.G.H. Lammertink. Inelastic non-Newtonian flow over heterogeneously slippery surfaces. *Phys. Rev. E*, 95(2):023105, 2017.

[36] M.A. Dominguez-Lerma, G. Ahlers, and D.S. Cannell. Marginal stability curve and linear growth rate for rotating Couette–Taylor flow and Rayleigh–Bénard convection. *Phys. Fluids*, 27(4):856–860, 1984.

[37] R.C. DiPrima and P. Hall. Complex eigenvalues for the stability of Couette flow. *Proc. R. Soc. Lond. A*, 396(1810):75–94, 1984.

[38] S. Chandrasekhar. *Hydrodynamic and hydromagnetic stability*. Dover Publications, 1981.

[39] O. Crumeyrolle, I. Mutabazi, and M. Grisel. Experimental study of inertioelastic Couette–Taylor instability modes in dilute and semidilute polymer solutions. *Phys. Fluids*, 14(5):1681–1688, 2002.

[40] K. Fujimura and S. Yamada. Hexagons and triangles in the Rayleigh-Bénard problem: quintic-order equations on a hexagonal lattice. *Proc. R. Soc. A*, 464:2721–2739, 2008.

[41] S.C. Generalis and K. Fujimura. Range of validity of weakly nonlinear theory in the Rayleigh-Bénard problem. *J. Phys. Soc. Jpn*, 78:1–11, 2009.

[42] B. Dubrulle and F. Hersant. Momentum transport and torque scaling in Taylor-Couette flow from an analogy with turbulent convection. *Eur. Phys. J. B*, 26(3):379–386, 2002.

[43] B. Eckhardt, S. Grossmann, and D. Lohse. Torque scaling in turbulent Taylor-Couette flow between independently rotating cylinders. *J. Fluid Mech.*, 581:221–250, 2007.

[44] A. Esmael, C. Nouar, A. Lefevre, and N. Kabouya. Transitional flow of a non-Newtonian fluid in a pipe: Experimental evidence of weak turbulence induced by shear-thinning behavior. *Phys. Fluids*, 22(10):101701, 2010.

[45] R.J. Donnelly and N.J. Simon. An empirical torque relation for supercritical flow between rotating cylinders. *J. Fluid Mech.*, 7(3):401–418, 1960.

[46] M. Bouteraa, C. Nouar, E. Plaut, C. Métivier, and A. Kalck. Weakly nonlinear analysis of Rayleigh–Bénard convection in shear-thinning fluids: nature of the bifurcation and pattern selection. *J. Fluid Mech.*, 767:696–734, 2015.

[47] M. Bouteraa and C. Nouar. Weakly nonlinear analysis of Rayleigh-Bénard convection in a non-Newtonian fluid between plates of finite conductivity: Influence of shear-thinning effects. *Phys. Rev. E*, 92(6):063017, 2015.

[48] H. Fasel and O. Booz. Numerical investigation of supercritical Taylor-vortex flow in a wide gap. *J. Fluid Mech.*, 138:21–52, 1984.

[49] D. Coles. Transition in circular Couette flow. *J. Fluid Mech.*, 21(3):385–425, 1965.

[50] R. Meyer-Spasche and H.B. Keller. Some bifurcation diagrams for Taylor vortex flows. *Phys. Fluids*, 28(5):1248–1252, 1985.

[51] O. Crumeyrolle, A. Latrache, I. Mutabazi, and A.B. Ezersky. Instabilities with shear-thinning polymer solutions in the Couette-Taylor system. In *J. Phys. Conf. Ser.*, volume 14, page 78.

IOP Publishing, 2005.